Doctoral Dissertation (Censored)
博士論文 (要約)

Evolution of Low- and Intermediate-mass Stars with Physics beyond the Standard Model
(小・中質量星の進化を用いた標準模型を超えた物理の探索)

A Dissertation Submitted for the Degree of Doctor of Philosophy

December 2020
令和 2 年 12 月博士 (理学) 申請

Department of Astronomy, Graduate School of Science, The University of Tokyo
東京大学大学院理学系研究科天文学専攻

Kanji Mori
森　寛治

Abstract

The Standard Model (SM) of particle physics provides the fundamental framework of elementary particles and interactions between them. Although it explains most results of terrestrial experiments, the SM is still on the way to the Theory of Everything. In order to search for a hint of physics beyond the SM, stars have been used as a probe of new physics which complements terrestrial experiments. In this thesis, I study the effects of the neutrino magnetic moment (NMM) and the large extra dimensions (LEDs) on low- and intermediate-mass stars.

Observations of neutrino oscillation have revealed that neutrinos are massive, although their mass is still unknown. Particle theories predict that such massive neutrinos have a magnetic moment. The SM with Dirac neutrinos predicts NMM of $\sim 10^{-19}\mu_{\rm B}$, where $\mu_{\rm B}$ is the Bohr magneton. This value is so small that terrestrial experiments and astrophysical observations cannot find its signature in near future. However, some theories beyond the SM predict that NMM can be as high as $\sim 10^{-12}\mu_{\rm B}$. Since its value is model-dependent, measurement of NMM is a key to physics beyond the SM. NMM has been explored by neutrino-electron scattering experiments, but it is desirable to search for astrophysical signatures of NMM to obtain tighter limit.

Gravity is another open problem in particle physics. Since it is difficult to quantize it, gravity is not included in the SM. Also, the reason why gravity is much weaker than the other interactions is not known. In order to solve this hierarchy problem, the idea of LEDs has been discussed. If n extra dimensions are compactified, the gravitational scale in the $(n+4)$-spacetime can be as low as the electroweak scale. LEDs have been explored by torsion balance experiments because they modify the inverse-square law. Also, Kaluza-Klein (KK) gravitons excited by LEDs have been searched by high-energy collider experiments. KK gravitons emitted from hot plasma potentially affect stellar evolution.

In Chapter 2, I study the effects of NMM and LEDs on intermediate-mass stars which form a blue loop on the Hertzsprung-Russell diagram during central helium burning. Since morphology of the blue loop is sensitive to input physics, it is expected that new physics also affects the evolution of intermediate-mass stars. If neutrinos have a finite magnetic

moment, an extra energy loss is induced by neutrino emission. Similarly, LEDs induce an energy loss from stellar plasma because of KK graviton emission. I implement additional energy losses induced by NMM and LEDs in a stellar evolution code and calculate the evolution of intermediate-mass stars. I find that the NMM leads to elimination of the blue loops during core helium burning. Some of stars in the blue loop are observed as a Cepheid variable when they cross the instability strip. In order for Cepheids to exist, the NMM should be smaller than the range $\sim 2\times10^{-10}$ to $4\times10^{-11}\mu_{\rm B}$ depending on the $^{12}{\rm C}(\alpha,\ \gamma)^{16}{\rm O}$ reaction rates.

LEDs are also explored in my study. Since the $n = 1$ model is clearly excluded by the square-inverse law on a large scale, I focused on the $n = 2$ case which is the simplest possible model. It is found that the fundamental scale in the (4+2)-spacetime should be larger than $\sim$ 2 to 5 TeV in order for the blue loop not to be eliminated. The constraints given by intermediate-mass stars are found to be weaker than the current experimental and astrophysical limits, but they offer an independent method to explore new physics.

In Chapter 3, I study the effect of NMM on the lithium abundance in low-mass stars. This part is motivated by a recent study that discovered ubiquitous lithium production in advanced evolutionary stages of low-mass stars. Since lithium is easily destroyed when it is conveyed to the inner hot region, the high surface lithium abundance has not been predicted by stellar theories. In order to mitigate this problem, I applied the effect of the NMM on the low-mass stellar evolution. Because of the additional energy loss, a more massive and smaller helium core is formed at the tip of the red giant branch. The smaller core leads to a less dense envelope. As a result, thermohaline mixing at the bottom of the envelope becomes more active and ^{7}Be produced in the hydrogen burning shell is conveyed to the convective envelope. The lithium abundance in red clump stars hence becomes larger when the NMM is considered. I conclude that the lithium problem is mitigated when the NMM of $\sim (2-5)\times10^{-12}\mu_{\rm B}$ is adopted. Although this value is higher than the tightest upper limit that comes from stellar evolution, the constraint is not robust because it can depend on numerical codes for stellar evolution which are used to compare stellar models with observed stars. Also, additional energy losses can be induced by other physics including coupling between axion-like particles and electrons. This result opens up a new possibility of mitigating the lithium problem with additional energy losses induced by physics beyond the SM.

Contents

Chapter 1

Introduction

1.1 Astrophysical Objects as a Laboratory of Fundamental Physics

The Universe has been a laboratory for contemporary physics since the dawn of modern science. In the seventeenth century, Johannes Kepler discovered his empirical laws (Kepler, 1609, 1619) on the planetary motion from careful analysis of Tycho Brahe's astronomical data. Kepler's laws provided an observational support for Classical Mechanics, which appeared in *Philosophiæ Naturalis Principia Mathematica* (Newton, 1687) written by Issac Newton.

In the twentieth century, Albert Einstein constructed the Theory of Relativity (Einstein, 1905, 1916a). Some of the earliest observational evidence of Relativity came from objects in the Solar System. Einstein successfully explained anomalous precession of Mercury with his theory (Einstein, 1915), which had been an open problem since the previous century (Le Verrier, 1859). In 1919, Arthur Eddington observed stars during a Solar eclipse and discovered bending of light caused by the Solar gravitational field (Dyson, Eddington & Davidson, 1920) as predicted by the General Theory of Relativity (Einstein, 1915). Einstein predicted the existence of gravitational waves (GWs) as well (Einstein, 1916b). Because of difficulties in detecting them, he could not see his prediction verified by observations. However, in 1975, Alan Hulse and Joseph Taylor found that the orbital decay of a binary pulser PSR B1913+16 is consistent with the prediction of the energy loss by the GW emission (Hulse & Taylor, 1975). This was the first indirect evidence of the existence of GWs. Recently, the first GW event GW150914 from a black hole binary merger was detected by the Laser Interferometer Gravitational-Wave Observatory (Abbott et al., 2016). This discovery was the first direct evidence of the existence of GWs and opened up the new field of GW and multi-messenger astronomy.

This kind of interplay between fundamental physics and astronomy has happened in stel-

lar physics as well. In the nineteenth century, Hermann von Helmholtz and William Thomson proposed the gravitational contraction as a major energy source of the Sun. However, the Kelvin-Helmholtz mechanism can support the Sun only for ~ 30 Myr, so an alternative mechanism was needed. Eddington came up with the idea of nuclear fusion of hydrogen (Eddington, 1920), but the quantum theory of nuclear reactions was immature at that time, so he could not show that such reactions occur in the stellar interior. Later, George Gamow developed the quantum theory of nuclear fusion (Gamow, 1928). The theory was applied to stars by astrophysicists including Hans Bethe (e.g. Atkinson, 1931; Gamow, 1938; Bethe, 1939) and the outline of stellar nuclear energy generation was understood. The classical results on nucleosynthesis in the Universe were reviewed in the celebrated B^2FH paper written by Margaret Burbidge, Geoffrey Burbidge, William Fowler, and Fred Hoyle (Burbidge et al., 1957). The research field of nuclear astrophysics is still active in the present day and is developing as an intersection of astronomy and theoretical and experimental nuclear physics (e.g. Bertulani & Kajino, 2016; Arnould & Goriely, 2020).

The most fundamental paradigm of modern physics is the Standard Model (SM) of particle physics. The model includes seventeen kinds of elementary particles shown in Fig. 1.1. According the SM, fermions are classified into two categories: quarks and leptons. Quarks are engaged in the strong interaction and form baryons and mesons. On the other hand, leptons are engaged in the weak interaction. The interactions between particles are mediated by the gauge bosons.

Almost all ground experiments can be understood within the framework of the SM and astrophysical discussions are usually based on the SM as well. In spite of its succuss, the SM cannot be the Theory of Everything because it has several problems. One is that the SM treats neutrinos as a massless particle, while they have finite masses in reality. This point will be discussed in Section 1.2. Another problem is that the SM does not explain gravity. In particular, the reason why gravity is much weaker than the other interactions is not understood. In order to solve this hierarchy problem, particle theorists proposed the idea of extra dimensions. This will be discussed in the next Section 1.3.

1.2 Magnetic Moment of Neutrinos

Neutrinos are neutral leptons which are included in the SM. They play important roles not only in particle physics but also in astrophysics. For example, core-collapse supernovae are thought to explode because of interactions between the background matter and neutrinos (e.g. Sato, 1975). Also, the neutrino-antineutrino annihilation is one of possible mechanisms to power relativistic jets in γ-ray bursts (e.g. Eichler et al., 1989).

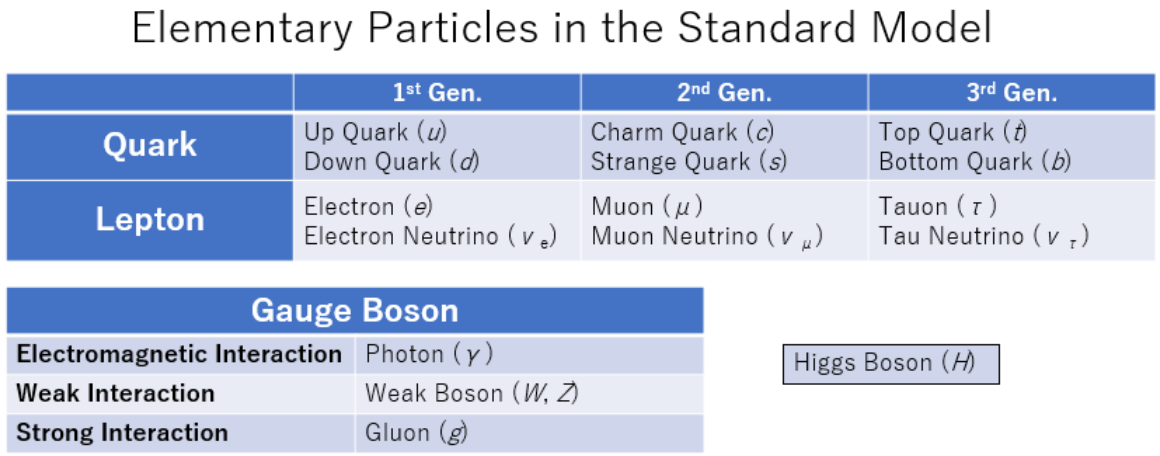

Fig. 1.1 The list of elementary particles included in the SM.

Historically, the idea of neutrinos were introduced by Wolfgang Pauli to explain continuous spectra of β-decays in 1930. In 1956, Clyde Cowan and Frederick Reines performed an experiment to discover $\bar{\nu}_e$ from a reactor (Cowan et al., 1956), focusing on the reaction with a proton in water: $\bar{\nu}_e + p \to n + e^+$. They succeeded in detecting neutrons and positrons which are produced by this reaction and confirmed the existence of neutrinos. The other types of neutrinos, muon and tau neutrinos, were discovered in 1962 and 2001, respectively (Danby et al., 1962; DONUT Collaboration et al., 2001).

In the SM, neutrinos are treated as massless particles. However, the flavor oscillation of atmospheric neutrinos was discovered by Super-Kamiokande (Fukuda et al., 1998). Since it happens only if neutrinos are massive, the neutrino oscillation undoubtedly shows the massive nature of neutrinos. Exploring the mass of neutrinos is hence a key to physics beyond the SM. As we see later, particle theories predict that massive neutrinos have magnetic moments, which potentially affect the stellar evolution.

Let us discuss possible mechanisms of the neutrino mass. When we introduce the Dirac mass term, we have to add a right-handed neutrino ν_R to the SM Lagrangian. Then the Yukawa term can be written as

$$\mathcal{L}_Y = -yH^0\overline{\nu_R}\nu_L + \text{h.c.}, \tag{1.1}$$

where ν_L is the left-handed neutrino, H^0 is the neutral Higgs boson, and y is the Yukawa coupling constant. The Higgs mechanism (Higgs, 1964; Englert & Brout, 1964) produces the Dirac mass term

$$\mathcal{L}_D = -yv\overline{\nu_R}\nu_L + \text{h.c.}, \tag{1.2}$$

where $v = 174$ GeV is the vacuum expectation value of the Higgs field. The neutrino mass is then written as $m_{\rm D} = yv$. If we assume $m_{\rm D} \sim 0.1$ eV, the Yukawa coupling is $y \sim 10^{-12}$. This tiny value of y looks unnatural and motivates us to consider another possibility, namely the Majorana mass term. The Majorana term for left-handed neutrinos is written as

$$\mathcal{L}_{\rm L} = -\frac{m_{\rm L}}{2}\overline{\nu_{\rm L}^{c}}\nu_{\rm L} + \text{h.c.} \tag{1.3}$$

The origin of this term is not known. The most natural mechanism is the so-called seesaw mechanism (Yanagida, 1980; Mohapatra & Senjanovic, 1980; Schechter & Valle, 1980), which concludes that $m_{\rm L} = m_{\rm D}^2/m_{\rm R}$. Here $m_{\rm R}$ is the Majorana mass of right-handed neutrinos. If we assume that $m_{\rm D}$ is similar to the muon mass and $m_{\rm L} \sim 0.1$ eV, the mass of right-handed neutrinos is estimated to be $m_{\rm R} \sim 10^8$ GeV.

In order to determine the nature of the neutrino mass, experimentalists have searched the neutrinoless double β-decay: ($0\nu\beta\beta$; Zyla et al., 2020)

$$(N,\ Z) \rightarrow (N,\ Z+2) + 2e^{-}. \tag{1.4}$$

If neutrinos are Majorana, this decay mode is allowed because neutrinos and antineutrinos are identical. At the time of writing of this thesis, the $0\nu\beta\beta$ has not been detected by any experiment. Recent results of KamLAND-Zen experiment argue that the half-life of the ^{136}Xe $0\nu\beta\beta$ should be longer than 1.07×10^{26} yr and the effective Majorana mass should be lower than 61-165 meV (Gando et al., 2016). Also, the absolute mass of neutrinos have been pursued experimentally, although only upper limits have been obtained by current studies. Recently, the end part of the β-decay spectrum of tritium was measured by the KATRIN (Karlsruhe Tritium Neutrino) experiment (Aker et al., 2019). They gave an upper limit < 1.1 eV on the effective ν_e mass.

The massive nature of neutrinos gives rise to electromagnetic properties (e.g. Giunti & Studenikin, 2015; Balantekin & Kayser, 2018). Shrock (1982) evaluated the neutrino magnetic moment (NMM) $\mu_{kj}^{\rm D}$ using the Weinberg-Salam theory with massive Dirac neutrinos. They obtained

$$\mu_{kj}^{\rm D} = \frac{3eG_{\rm F}}{16\sqrt{2}\pi^2}(m_k + m_j)\left(\delta_{kj} - \frac{1}{2}\sum_l U_{lk}^{*}U_{lj}\frac{m_l^2}{m_{\rm W}^2}\right), \tag{1.5}$$

where $G_{\rm F}$ is the Fermi coupling constant, $m_{\rm W}$ is the mass of the weak boson, U is the Pontecorvo-Maki-Nakagawa-Sakata matrix (Maki, Nakagawa & Sakata, 1962), and m_l is the mass of the charged lepton. It easily follows that the diagonal magnetic moment is given as

$$\mu_{kk}^{\rm D} = \frac{3eG_{\rm F}m_k}{8\sqrt{2}\pi^2} = 3.2 \times 10^{-19}\left(\frac{m_k}{\rm eV}\right)\mu_{\rm B}, \tag{1.6}$$

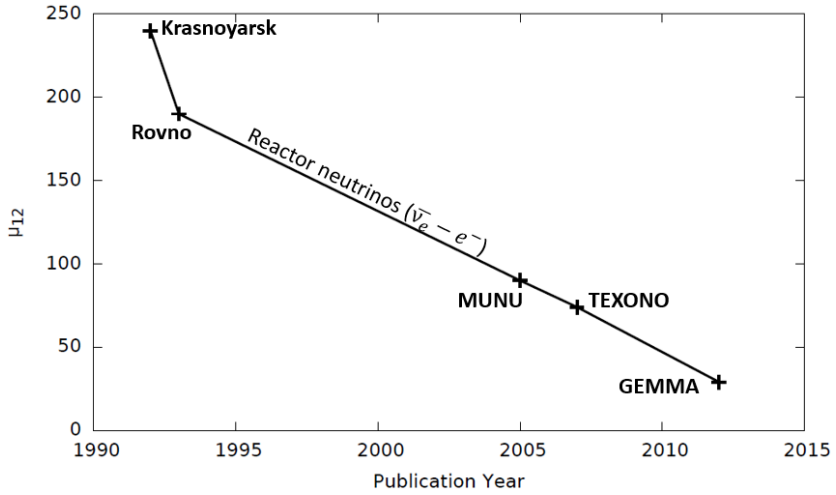

Fig. 1.2 The upper limit on $\mu_{12} = \mu/(10^{-12}\mu_B)$ which has been obtained by recent reactor $\bar{\nu}_e - e^-$ experiments.

where μ_B is the Bohr magneton. On the other hand, Majorana neutrinos do not have the magnetic moment, i.e. $\mu^M_{kk} = 0$ (Shrock, 1982). Since the magnetic moment given by Eq. (1.6) is tiny, it is difficult to detect it with ground experiments or astrophysical discussion. However, some of models beyond the SM predict much higher magnetic moment. For example, the minimal supersymmetric SM (Aboubrahim et al., 2014) predicts $\mu \sim (10^{-12} - 10^{-14})\mu_B$.

The model-dependence of the NMM makes it a key to beyond-standard physics. Because of its importance, the NMM has been pursued experimentally. The earliest measurement was performed by Cowan, Reines & Harrison (1954), who obtained a constraint $\mu < 10^{-7}\mu_B$. Fig. 1.2 summarizes the upper limits on the NMM obtained by recent reactor $\bar{\nu}_e - e^-$ experiments (Vidyakin et al., 1992; Derbin et al., 1993; Daraktchieva et al., 2005; Wong et al., 2007). The most stringent limit $\mu < 2 \times 10^{-11}\mu_B$ comes from the Germanium Experiment on Measurement of Magnetic Moment of Antineutrino (GEMMA; Beda et al., 2013). In GEMMA, neutrinos from Kalinin Nuclear Power Plant in Russia were used. The $\bar{\nu}_e - e^-$ cross sections are given by the sum of the weak ($d\sigma_W/dT$) and electromagnetic ($d\sigma_{EM}/dT$) components.

$$\frac{d\sigma_W}{dT} = \frac{G_F^2 m_e}{2\pi}\left(4x^2 + (1+2x^2)^2\left(1-\frac{T}{E}\right)^2 - 2x^2(1+x^2)\frac{m_e T}{E^2}\right) \tag{1.7}$$

$$\frac{d\sigma_{EM}}{dT} = \pi r^2\left(\frac{\mu}{\mu_B}\right)^2\left(\frac{1}{T}-\frac{1}{E}\right) \tag{1.8}$$

Here T is the electron recoil energy, E is the incident neutrino energy, G_F is the Fermi coupling constant, m_e is the electron mass, r is the classical electron radius, $x = \sin\theta_W$ is

the Weinberg parameter. These equations show that the NMM can be measured from the $\bar{\nu}_e - e^-$ spectrum. In GEMMA, a high purity germanium detector was used to measure $d\sigma/dT$.

Eqs. (1.7) and (1.8) can be used to constrain the NMM with the Solar neutrinos too. The Super-Kamiokande Collaboration (Liu et al., 2004) and the Borexino Collaboration (Arpesella et al., 2008) obtained the constraints of $\mu < 1.1 \times 10^{-10} \mu_B$ and $\mu < 5.4 \times 10^{-11} \mu_B$, respectively.

The $\bar{\nu}_e - e^-$ scattering flips the neutrino helicity. It is hence possible that a left-handed Dirac neutrino is transformed into a right-handed sterile neutrino. This process potentially prevent neutrino-driven explosion of core-collapse supernovae. Ayala, D'olivio & Torres (1999) estimated that the energy Q_{ν_R} carried away by sterile neutrinos is

$$Q_{\nu_R} = \left(\frac{\mu}{\mu_B}\right)^2 (0.7 - 4.3) \times 10^{76} \text{ erg/s}. \tag{1.9}$$

In order for the neutrino-driven explosion mechanism to work, Q_{ν_R} should be lower than 10^{53} erg/s. This leads to a constraint $\mu < (0.1 - 0.4) \times 10^{-11} \mu_B$.

The NMM has been constrained by astronomical observations as well. Evolution of low-mass stars are sensitive to the additional energy loss induced by the NMM. The neutrino emission rate in stellar plasma is enhanced by the processes shown in Fig. 1.3. Haft, Raffelt & Weiss (1994) calculated the plasmon decay rate as a function of the density ρ and the temperature T. Their result is

$$\epsilon^{\mu}_{\text{plas}} = 0.318 \left(\frac{\omega_{\text{pl}}}{10 \text{ keV}}\right)^{-2} \left(\frac{\mu}{10^{-12} \mu_B}\right)^2 \epsilon_{\text{plas}}, , \tag{1.10}$$

where ϵ_{plas} is the standard plasmon decay rate (Itoh et al., 1996) and ω_{pl} is the plasma frequency written as (Raffelt, 1996)

$$\omega_{\text{pl}} = 28.7 \text{ eV} \frac{(Y_e \rho)^{\frac{1}{2}}}{(1 + (1.019 \times 10^{-6} Y_e \rho)^{\frac{2}{3}})^{\frac{1}{4}}}. \tag{1.11}$$

Here Y_e is the electron fraction. The pair production rate of neutrinos are given as (Heger et al., 2009)

$$\epsilon^{\mu}_{\text{pair}} = 1.6 \times 10^{11} \text{ erg g}^{-1} \text{ s}^{-1} \left(\frac{\mu}{10^{-10} \mu_B}\right)^2 \frac{e^{-\frac{118.5}{T_8}}}{\rho_4}, \tag{1.12}$$

where $T = T/(10^8 \text{ K})$ and $\rho_4 = \rho/(10^4 \text{ g/cm}^3)$. These processes will be discussed in Appendices A and B in detail.

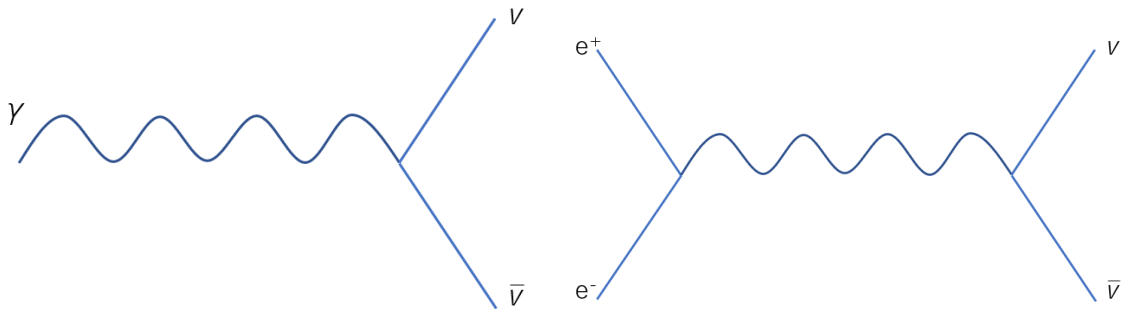

Fig. 1.3 The Feynman diagrams that show (left) the plasmon decay and (right) the pair creation induced by the NMM.

The enhanced energy loss rates have been applied to low-mass stellar models to constrain the NMM (Bernstein, Ruderman & Feinberg, 1963; Raffelt & Dearborn, 1988; Raffelt, 1990; Viaux et al., 2013a,b). Since the luminosity of stars at the tip of the red giant branch (TRGB) becomes larger because of the additional energy loss, it is possible to constrain the NMM with low-mass stars. The most recent study (Arceo-Díaz et al., 2015) implemented the effect of the NMM in models of low-mass red giants (RGs) and compared them with stars at the TRGB in a globular cluster ω Cen. They obtained an upper limit $\mu < 2{\times}10^{-12}\mu_{\rm B}$.

The NMM can induce the radiative decay of neutrinos. If a neutrino $\nu_{\rm i}$ is heavier than $\nu_{\rm f}$, $\nu_{\rm i}$ can emit a photon to produce $\nu_{\rm f}$. The decay photon affects the spectrum of the cosmic microwave background. The constraint from the cosmic microwave background is $\mu < 3 \times 10^{-11}\mu_{\rm B}({\rm eV}/m_\nu)^{2.3}$ (Ressell & Turner, 1990).

It is notable that the neutrino radiative decay can also affect Big Bang nucleosynthesis (BBN) (e.g. Terasawa, Kawasaki & Sato, 1988; Kusakabe et al., 2013). BBN offers tight constraints on the mass and the lifetime of massive unstable neutrinos. Since the primordial abundances of light elements are determined precisely by recent astronomical observations, the non-standard BBN scenarios are actively studied from the theoretical viewpoints.

1.3 Large Extra Dimensions

The idea of extra dimensions was proposed by Theodor Kaluza and Oskar Klein (Kaluza, 1921; Klein, 1926). They constructed a 5-dimensional theory with the generalized Einstein-Hilbert action

$$S = -\frac{1}{16\pi\hat{G}}\int \hat{R}\sqrt{-\hat{g}}d^4xdy, \tag{1.13}$$

where the hats show 5-dimensional quantities. The classic Kaluza-Klein (KK) theory naturally unifies gravity and electromagnetism, but it predicts that the electron mass would be the Planck scale (Overduin & Wesson, 1997), which clearly contradicts the reality.

Later, Arkani-Hamed, Dimopoulos & Dvali (1998) proposed the idea of the large extra dimensions (LEDs). They considered compactified extra dimensions with the size of ∼mm. They assumed that only gravity can propagate in the extra dimensional space. In this theory, the gravitational potential $V(r)$ between masses m_1 and m_2 is given by

$$V(r) = -G^{(3+n)}\frac{m_1 m_2}{r^{1+n}} \quad (r < \Lambda), \tag{1.14}$$

where $G^{(3+n)}$ is the gravitational constant with n extra dimensions, when the distance r between the masses is smaller than the size Λ of the extra dimensions. On the other hand, we can show from Gauss' law that

$$V(r) = -G^{(3+n)}\frac{m_1 m_2}{r}\frac{1}{V_n} \quad (r > \Lambda), \tag{1.15}$$

where V_n is the volume of the extra dimensions. Comparison between the Newtonian law of gravity and Eq. (1.15) shows that $G^{(3)} = G^{(3+n)}/V_n$, where $G^{(3)}$ is the usual gravitational constant. This relation implies that $E_{(n)}^{n+2} \propto E_{\rm Pl}^2/V_n$, where $E_{(n)}$ is the true Planck scale in the $(4+n)$-dimensional spacetime and $E_{\rm Pl} \sim 10^{19}$ GeV is the Planck scale which we know. It is seen that $E_{(n)}$ can be down to the electroweak scale if V_n is sufficiently large.

How large should the extra dimensions be? Assuming that $E_{(\rm n)} \sim 1$ TeV and $V_n \sim \Lambda^n$, we can estimate the values of Λ that can solve the hierarchy problem. In the case of $n = 1$, 2, and 3, the size of the extra dimension should be $\Lambda \sim 10^{13}$ m 10^{-3} m, and 10^{-8} m, respectively. The $n = 1$ case clearly contradicts observations, because Λ is so large that gravity deviates from the inverse-square law on the scale of the Solar System. However, the $n \geq 2$ cases still survive, so studying them are worthwhile. In this thesis, we mainly focus on the $n = 2$ case, which is the simplest possible model.

If the LEDs exist, the gravitational potential deviates from the square-inverse law on the small scale. The gravitational force on the mm scale have been measured using a torsion pendulum (Long, Chan & Price, 1999; Hoyle et al., 2001; Chiaverini et al., 2003; Hoyle et al., 2004; Smullin et al., 2005; Kapner et al., 2007; Tu et al., 2007; Geraci et al., 2008; Sushkov et al., 2011; Yang et al., 2012; Murata & Tanaka, 2015; Tan et al., 2016, 2020), but deviation from the square-inverse law has not been discovered. The most recent torsion experiment (Lee et al., 2020) concludes that the inverse-square law holds down to 52 μm. A typical setup of such torsion balance experiments is schematically shown in Fig. 1.4.

The LEDs give rise to the KK modes of gravitons $G_{\rm KK}$ with masses $m_{\boldsymbol{n}^2} = |\boldsymbol{n}|^2/\Lambda^2$. Collider experiments have been performed to search for the missing energy due to the production of KK gravitons (Aaltonen et al., 2008; Aad et al., 2011, 2013; Sirunyan et al., 2018; Aaboud et al., 2018). The Compact Muon Solenoid (CMS) experiment at the Large

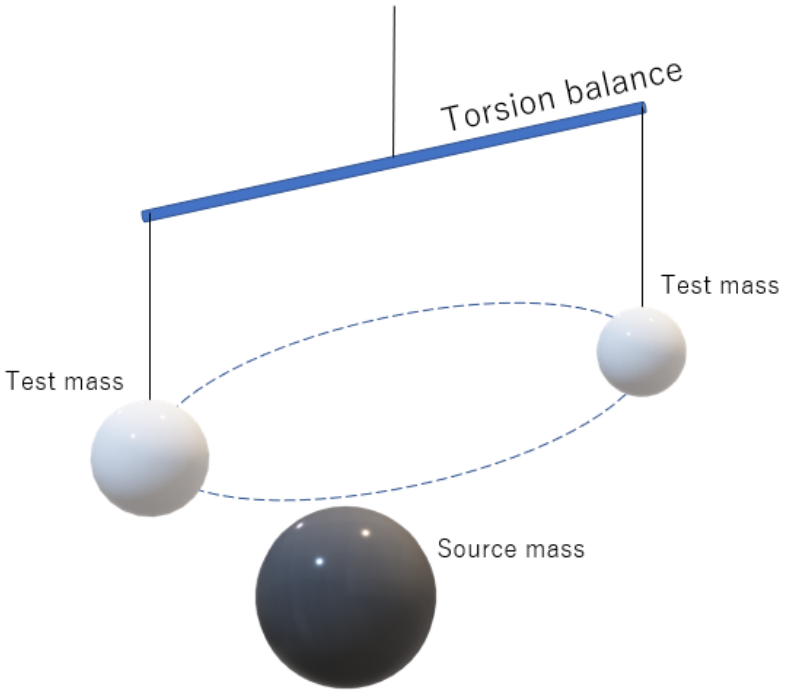

Fig. 1.4 A schematic picture for a typical setup of torsion balance experiments.

Hadron Collider reports $M_{\rm D} > 9.9$ TeV for the $n = 2$ model (Sirunyan et al., 2018), where $M_{\rm D}$ is the fundamental scale defined as

$$M_{\rm Pl}^2 = \Lambda^n M_{\rm D}^{n+2}. \tag{1.16}$$

The current constraints on n and $M_{\rm D}$ are summarized in Fig. 1.5. It is seen that the torsion and collider experiments give comparable constraints when $n = 2$, while the collider experiments become advantageous when $n > 3$.

LEDs can be constrained by astrophysical and cosmological ways as well. Detection of a neutrino burst from SN 1987A at Kamiokande (Hirata et al., 1987) and the IMB detector (Bionta et al., 1987) revealed that a lot of neutrinos are emitted from a core-collapse supernova. If the graviton emission in a supernova explosion is too efficient, the expected number of supernova neutrinos becomes lower and thus the observed neutrino counts cannot be explained. Hanhart et al. (2001) obtained a limit $\Lambda < 0.66$ μm from the neutrinos from SN 1987A. Gravitons produced by a supernova are expected to be bound in a neutron star and decays to photons. Fermi-LAT Collaboration et al. (2012) set a limit on the γ-ray flux from γ-ray quiet neutron stars and obtained a limit $M_{\rm D} > 230$ TeV. The radiative decay of gravitons will contribute to the cosmic γ-ray radiation and Hall & Smith (1999) obtained a limit $M_{\rm D} > 110$ TeV.

KK gravitons can be produced in stellar plasma as well. The new energy loss channel can

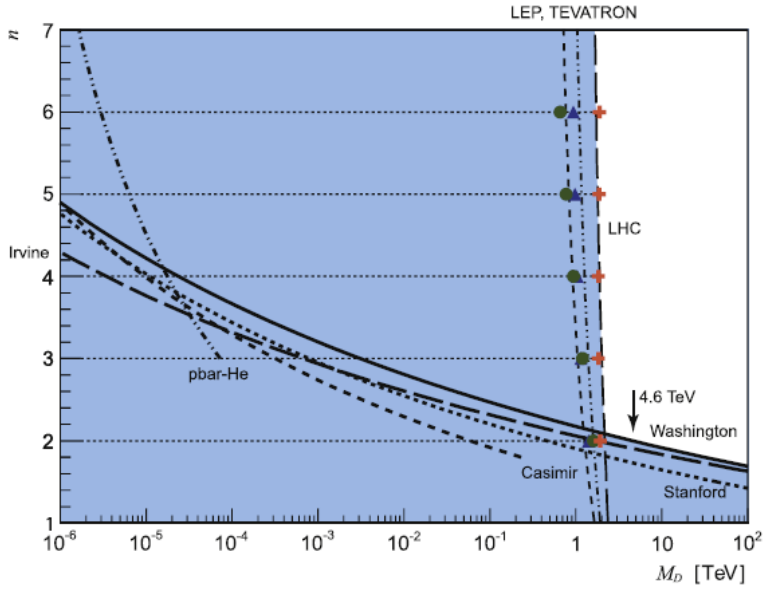

Fig. 1.5 The constraints on n and $M_{\rm D}$ given by the torsion and the collider experiments. This figure is reprinted from Fig. 12 in Murata & Tanaka (2015) with permission.

be used to constrain the LEDs in principle. The energy loss rate was calculated by Barger et al. (1999). In the stellar condition we are interested in, photon-photon annihilation, gravi-Compton-Primakoff scttering, and gravi-bremsstrahlung are effective processes. The energy loss rates due to these processes are evaluated as follows (Hansen et al., 2015):

1. Photon-photon annihilation ($\gamma + \gamma \to G_{\rm KK}$)

$$\epsilon_{\gamma\gamma} = 5.1 \times 10^{-9} T_7^9 \rho_6^{-1} \left(\frac{M_{\rm S} c^2}{1\ {\rm TeV}} \right)^{-4}\ {\rm erg\ g^{-1}\ s^{-1}} \tag{1.17}$$

2. Gravi-Compton-Primakoff scttering ($e^- + \gamma \to e^- G_{\rm KK}$)

$$\epsilon_{\rm GCP} = 4.5 \times 10^{-6} T_7^7 \left(\frac{M_{\rm S} c^2}{1\ {\rm TeV}} \right)^{-4}\ {\rm erg\ g^{-1}\ s^{-1}} \tag{1.18}$$

3. Gravi-bremsstrahlung ($e^- + N \to e^- + N + G_{\rm KK}$)

$$\epsilon_{\rm GB} = 5.8 \times 10^{-3} \bar{Z}_7^2 T_7^3 \left(\frac{M_{\rm S} c^2}{1\ {\rm TeV}} \right)^{-4}\ {\rm erg\ g^{-1}\ s^{-1}} \tag{1.19}$$

Here $T_7 = T/(10^7\ {\rm K})$, $\rho_6 = \rho/(10^6\ {\rm g\ cm^{-3}})$, and $\bar{Z}_7$ is the mean ion charge relative to nitrogen. $M_{\rm S}$ is the fundamental energy scale given by

$$M_{\rm S}^{-(n+2)} = \Omega_n M_{\rm Pl}^{-2} \Lambda^n, \tag{1.20}$$

where Ω_n is the n-dimensional spherical volume. Cassisi et al. (2000) applied these rates to the evolution of low-mass stars. They found that stars at the TRGB become luminous when the additional energy loss is considered. Comparison between the models and observed stars in a globular cluster gave a constraint $M_S > 3 - 4$ TeV.

1.4 Stellar Energy-loss Argument

Modern stellar physics tells us that stars are the result of all of the four fundamental interactions (i.e. gravity, electromagnetism, and strong and weak nuclear forces). Stars are bound by gravity, emit electromagnetic waves, and are powered by nuclear reactions. This fact enables us to use stars as a laboratory for new physics which cannot be tested by ground experiments (e.g. Raffelt, 1996). Such attempts can be divided into two classes. One is to use a large distance between stars and the Earth. Particles from stars may decay or oscillate during the propagation toward an observer. The most successful example of this method is the discovery of the flavor oscillation of the Solar neutrinos at the Sudbury Neutrino Observatory (Ahmad et al., 2001). The other method is to study the effect of new physics on stellar structure and evolution. One of the earliest examples for this method was performed by Katsuhiko Sato and Humitaka Sato (Sato & Sato, 1975). They considered a possible Higgs emission from central helium burning stars. If the Higgs mass is too small, the energy loss rate becomes so large that the lifetime of stars becomes shorter than observed. They argued that the Higgs mass should be larger than 0.36 MeV. Their lower limit is correct from modern points of view, as the Higgs mass is estimated to be 125 GeV (Zyla et al., 2020) by recent collider experiments.

Since then, the energy loss argument has been mainly applied to low-mass stars, because the luminosity of the brightest red giants and the lifetime of horizontal branch (HB) stars are sensitive to the additional energy loss. The structure of these stars is schematically shown in Fig. 1.6. In red giant branch (RGB) stars, a degenerate helium core is surrounded by a hydrogen burning shell. When the core mass reaches a critical value, the helium flash occurs and the core becomes non-degenerate. The star then starts stable core helium burning and evolves on the horizontal branch (HB).

It is possible to constrain the additional energy loss in low-mass stars with a simple analysis (Raffelt, 1996). In stars on the red giant branch, the helium core grows because of hydrogen shell burning. As the core mass grows, the radius of the core shrinks and the gravitational binding energy is released. If we treat the core as a white dwarf, the total

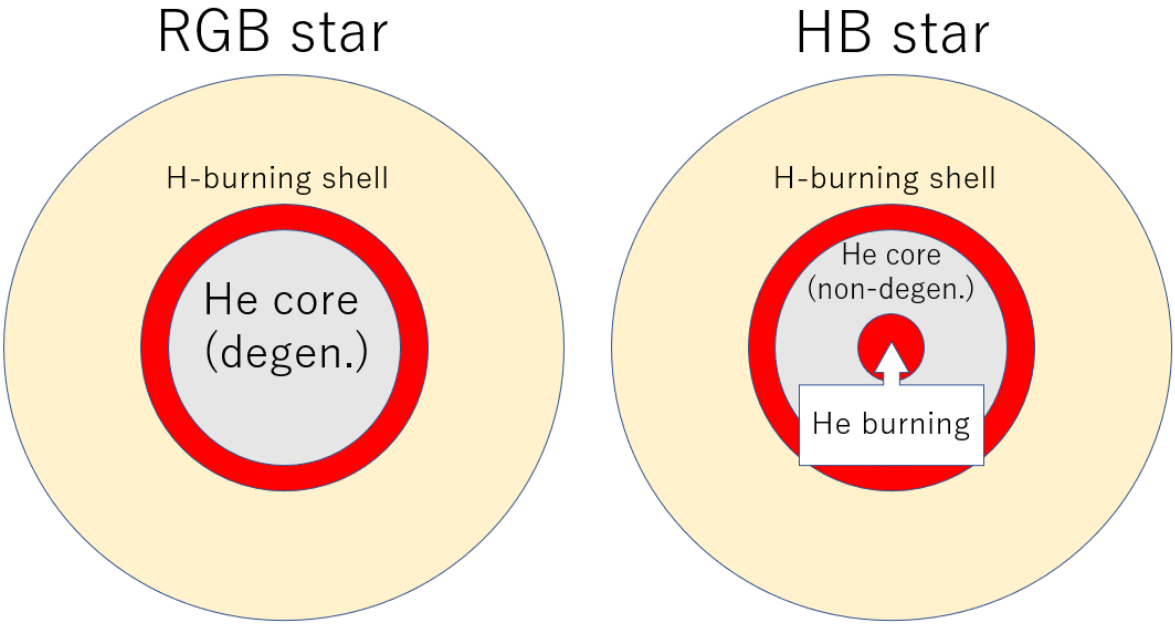

Fig. 1.6 The schematic structure of advanced evolutionary stages of low-mass stars. The radius is not to scale.

energy of the core is written as

$$E = -\frac{3}{7}\frac{GM_{\rm He}^2}{R_{\rm He}}, \tag{1.21}$$

where $M_{\rm He}$ is the helium core mass, $R_{\rm He}$ is the core radius, and G is the gravitational constant. The gravitational energy release is then estimated as

$$\epsilon_{\rm grav} = -\frac{\dot{E}}{M_{\rm He}} = \frac{G\dot{M}}{R_*}\left(\frac{M_{\rm He}}{M_\odot}\right), \tag{1.22}$$

where the M-R relation of a white dwarf $R = R_*(M_\odot/M)^{\frac{1}{3}}$ is used with $R_* = 8800$ km. If we put $M_{\rm He} = 0.5M_\odot$ and $\dot{M} = 0.8 \times 10^{-15} M_\odot$ s^{-1} for stars near the TRGB, we obtain $\epsilon_{\rm grav} \sim 100$ erg g^{-1} s^{-1}. If the additional energy loss ϵ_X is larger than $\epsilon_{\rm grav}$, the helium core mass at the TRGB becomes larger than the values estimated from observations. It is then concluded that $\epsilon_X < 100$ erg g^{-1} s^{-1}.

A similar argument can be applied to HB stars too. The number of HB stars in a globular cluster is determined by the duration $t_{\rm He}$ of central helium burning. If an additional energy loss ϵ_X is introduced, the duration is reduced by a factor of $L_{\rm He}/(L_X + L_{\rm He})$, where $L_{\rm He}$ is the luminosity of helium burning and L_X is the additional energy loss rate. It is known that $t_{\rm He}$ in the standard stellar model agrees with observational estimates within 10% (Raffelt, 1996). This leads to a constraint $L_X < 0.1L_{\rm He}$. Since the typical energy generation rate is $\epsilon_{\rm He} \approx 80$ erg/g/s, the additional energy loss is limited to $\epsilon_X < 10$ erg/g/s.

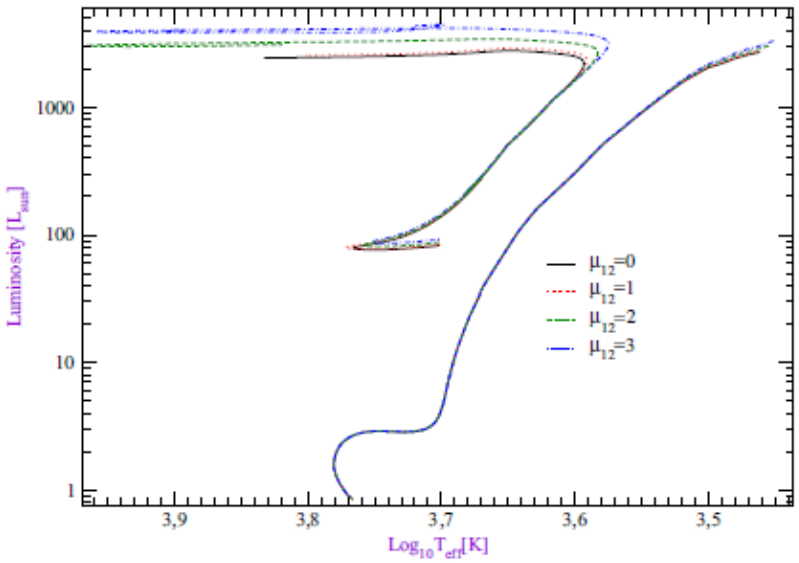

Fig. 1.7 The HR diagram of low-mass stars with the NMM $\mu = 0 - 3 \times 10^{-12}\mu_{\rm B}$, where $\mu_{\rm B}$ is the Bohr magneton. The metallicity is $Z = 0.01$. This figure is reprinted from Fig. 4 in Arceo-Díaz et al. (2015) with permission.

This effect of the additional energy loss on a modern stellar model is shown in Fig. 1.7, which is the Hertzsprung-Russell (HR) diagram of $1M_\odot$ stars (Arceo-Díaz et al., 2015) with different values of the NMM. It is seen that the luminosity at the TRGB becomes higher when the NMM is adopted. This prediction is compared with observations of globular clusters to constrain new physics. This method has been adopted to constrain various physics including the NMM (Bernstein, Ruderman & Feinberg, 1963; Raffelt & Dearborn, 1988; Raffelt, 1990; Viaux et al., 2013a,b; Arceo-Díaz et al., 2015), the large extra dimensions (Barger et al., 1999; Cassisi et al., 2000), and axion-like particles (Krauss et al., 1984; Dearborn et al., 1986; Raffelt & Dearborn, 1987; Ayala et al., 2014).

The additional energy loss can be constrained also by cooling of compact objects. Cooling of hot white dwarf (WD) is dominated by the neutrino emission due to the plasmon decay. If the energy is lost by a new physical process, it will be leave a trace in the luminosity function (Blinnikov & Dunina-Barkovskaya, 1994; Miller Bertolami, 2014; Hansen et al., 2015). The luminosity function $dN/dM_{\rm bol}$ is written as

$$\frac{dN}{dM_{\rm bol}} = -B\frac{dU/dM_{\rm bol}}{L_\gamma + L_\nu + L_X}, \tag{1.23}$$

where N is the number density of WDs, $M_{\rm bol}$ is the bolometric magnitude, U is the internal energy, L_γ is the electromagnetic luminosity, L_ν is the neutrino luminosity, and $B \approx 10^{-3}$ pc^{-3}Gyr^{-1} is the WD birthrate. A recent study (Hansen et al., 2015) obtained

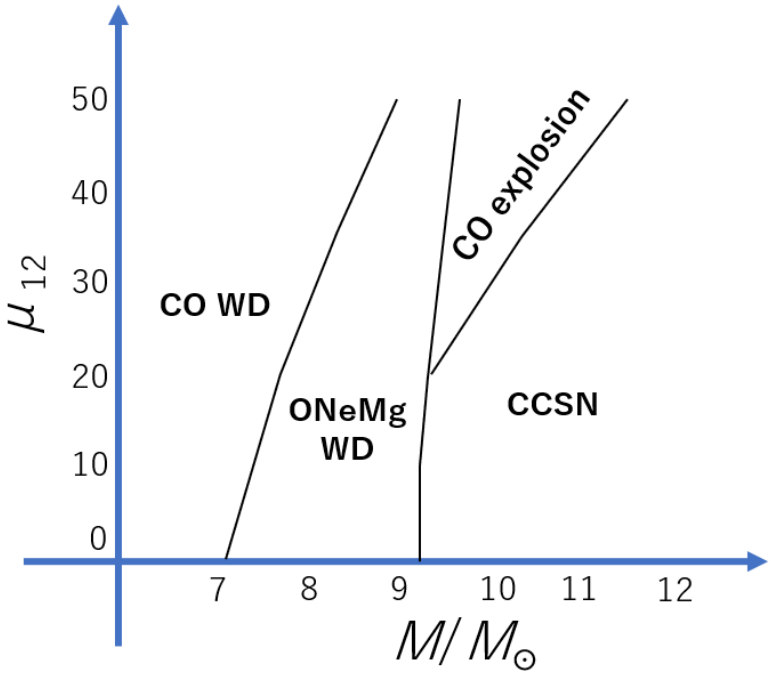

Fig. 1.8 The effect of the NMM on the fate of massive stars. This figure is drawn on the basis of the stellar evolution models shown in Heger et al. (2009).

constraints $\mu < 3.4 \times 10^{-12}\mu_B$ and $M_S > 0.54$ TeV using WDs in the globular cluster 47 Tucanae. Although the NMM can affects cooling of neutron stars in principle, Iwamoto et al. (1995) concluded that the constraint that can be obtained from neutron star cooling is $\mu < 5 \times 10^{-7}\mu_B$, which is much weaker than the constraints from low-mass stars and WDs.

The energy loss induced by new physics affects massive stars as well. Heger et al. (2009) studied the effect of the NMM on stars with 7-18$M_\odot$ and found that the fate of massive stars is significantly affected. Their result is summarized in Fig. 1.8. They showed that the NMM makes the threshold between a white dwarf and a core-collapse supernova more massive. Also, they predicted that $\sim 10M_\odot$ stars explode as "Type I.7" supernovae when the NMM is larger than $2\times10^{-11}\mu_B$, where μ_B is the Bohr magneton. Straniero et al. (2019) found that the energy loss induced by axion-like particles affects the initial mass-final luminosity relation of core-collapse supernova progenitors. It is difficult to constrain axions from this relation because of the current limited number of supernova samples. However, it is potentially a powerful tool to explore new physics when the number of samples is accumulated.

1.5 Summary: Constraints on the Neutrino Magnetic Moment and Large Extra Dimensions

In this Chapter, the concept of the NMM and LEDs was introduced and experimental and astrophysical constraints on them were explained. The current constraints on the NMM mentioned in this Chapter are summarized in Table 1.1. The most stringent experimental limit is obtained by reactor neutrinos and the most stringent astrophysical limit is obtained by the evolution of low-mass stars.

The current constraints on the model with two LEDs (i.e. $n = 2$) are summarized in Table 1.2. The most stringent experimental limit is obtained by the collider experiments and the most stringent astrophysical limit is obtained by non-detection of γ-rays from neutron stars.

In this thesis, I provide an independent method to constrain the NMM and the LEDs and point out that the additional energy loss induced by new physics can be a partial solution to the lithium problem in low-mass stars. In Chapter 2, I will discuss the effects of physics beyond the Standard Model on intermediate-mass stellar evolution. In Chapter 3, I will discuss the effects of beyond-standard physics on low-mass stars to explain the lithium abundance in red clump stars.

[*1] This value is not a limit. If the NMM in a range of $\mu_{12} = 2 - 5$ is assumed, the lithium abundance in low-mass red clump stars is significantly enhanced. As a result, discrepancy between stellar models and observed stars is mitigated.

Table. 1.1 Current experimental and astrophysical constraints on the NMM.

Method	Upper limit on μ_{12}	Reference
Reactor neutrino	29	Beda et al. (2013)
Solar neutrino	54	Arpesella et al. (2008)
Core-collapse supernova	1-4	Ayala et al. (2014)
Cosmic microwave background	$30(\mathrm{eV}/m_\nu)^{2.3}$	Ressell & Turner (1990)
White dwarf	3.4	Hansen et al. (2015)
Neutron star	5×10^5	Iwamoto et al. (1995)
Low-mass red giant	1.2	Capozzi & Raffelt (2020)
Intermediate-mass star	40-200	This work (Chapter 2)
Li abundance in low-mass stars	2-5[*1]	This work (Chapter 3)

Table. 1.2 Current experimental and astrophysical constraints on the LED model with $n = 2$.

Method	Upper limit on Λ [μm]	Reference
Collider	4.9	Sirunyan et al. (2018)
Tortion balance	30	Lee et al. (2020)
Core-collapse supernova	0.66	Hanhart et al. (2001)
Cosmic γ-ray background	4.0×10^{-2}	Hall & Smith (1999)
White dwarf	2×10^3	Hansen et al. (2015)
Neutron star	8.7×10^{-3}	Fermi-LAT Collaboration et al. (2012)
Low-mass red giant	40-70	Cassisi et al. (2000)
Intermediate-mass star	30-170	This work (Chapter 2)

Chapter 2

Evolution of Intermediate-mass Stars with the NMM and LEDs

インターネット公表に関する使用承認が出版社から得られないため、本章については、非公開。

“Elimination of the Blue Loops in the Evolution of Intermediate-mass Stars by the Neutrino Magnetic Moment and Large Extra Dimensions”
The Astrophysical Journal, 901, 115.

Chapter 3

Enhancement of Lithium in Red Clump Stars by the NMM

3.1 Introduction

Since ^{7}Li is a fragile nucleus which is easily destroyed by the proton capture reaction, its surface abundance reflects detailed stellar structure. In low-mass giants, stellar models predict the surface lithium depletion (Iben, 1967). However, spectroscopic surveys have shown that $\sim 1\%$ of giant stars have the lithium abundance as high as $A(\mathrm{Li}) = \log(\mathrm{Li/H}) + 12 > 1.5$ (Castilho et al., 2000; Gonzalez et al., 2009; Monaco et al., 2011; Kumar et al., 2011; Ruchti et al., 2011; Martell & Shetrone, 2013; Adamów et al., 2014; Casey et al., 2016; Yan et al., 2018; Smiljanic et al., 2018; Deepak & Reddy, 2019). This is a long-standing problem in my understanding of low-mass stars (Wallerstein & Sneden, 1982; Brown et al., 1989).

Stars in the RG branch and the red clump (RC) have the similar luminosity and the effective temperature, so the boundary between them is ambiguous in the Hertzsprung-Russell diagram. Some authors have suggested that a part of the lithium-rich giants are RC stars (Silva Aguirre et al., 2014; Monaco et al., 2014). Recent works (Singh, Reddy & Kumar, 2019; Singh et al., 2019; Kumar et al., 2020) distinguished RC stars from RGs in data of spectroscopic surveys with the help of asteroseismological data (Bedding et al., 2011; Vrard, Mosser & Samadi, 2016). They concluded that all of RC stars have the lithium abundances of $A(\mathrm{Li}) > -0.9$, which are higher than the predicted values by stellar models. This implies that a ubiquitous process produces ^{7}Li during or before central helium burning.

Kumar et al. (2020) pointed out that the lithium abundances in RC stars are distributed around $A(\mathrm{Li}) = 0.71$, while classical lithium-rich giants with $A(\mathrm{Li}) > 1.5$ account for only $\sim 3\%$ of RC stars. Fig. 3.1 is the histogram of $A(\mathrm{Li})$ in RC stars. In my study,

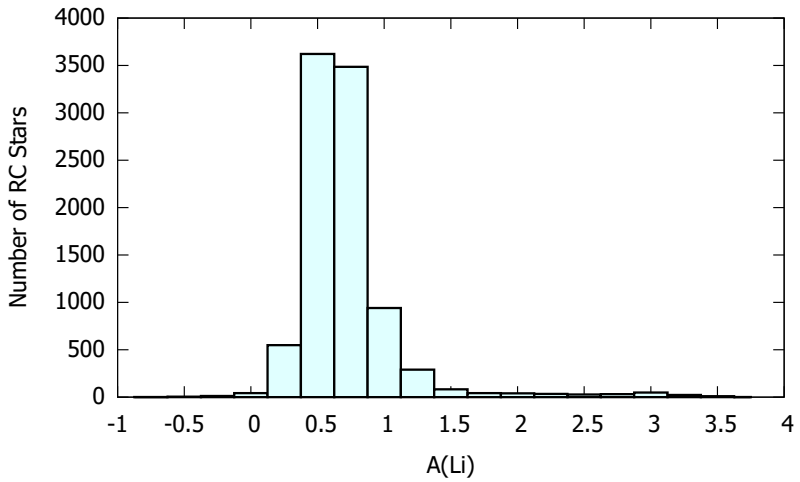

Fig. 3.1 The histogram of A(Li) in RC samples reported by Kumar et al. (2020). The total number of the RC samples is 9284.

I hypothesize that A(Li) in the majority with A(Li) $\sim$ 0.71 is enhanced by a ubiquitous process which occurs in all low-mass stars and the minority with A(Li) $>$ 1.5 is explained by other mechanisms which work only in specific types of stars. It should be noted that a recent observational study (Yan et al., 2020) found that 86% of lithium-rich giants with A(Li) $>$ 1.7 is RC stars. This motivates one to study possible mechanisms to produce such rare but extremely lithium-rich RC stars, although my work focuses on the peak of the A(Li) distribution.

The mechanism of the lithium enhancement is under debate. Some authors suggest engulfment of substellar objects which keep high lithium abundances (e.g. Siess & Livio, 1999; Lebzelter et al., 2012; Aguilera-Gómez et al., 2016). Others discuss in situ production by the Camelon-Fowler (CF) mechanism (Cameron & Fowler, 1971). In the hydrogen burning shell, ^{7}Be is produced via the ^{3}He(α, γ)^{7}Be reaction. The produced ^{7}Be is conveyed to the stellar surface and decays to ^{7}Li by the electron capture. In the standard model, the CF mechanism is insufficient to reproduce the abundance in lithium-rich giants. However, Casey et al. (2016) point out that extra mixing induced by the tidal interaction with a binary companion can drive the lithium production.

In order to explain the ubiquitous enhancement of lithium in RC stars, I introduce the additional energy loss induced by the NMM. The NMM induces the additional energy loss in stellar plasma (Haft, Raffelt & Weiss, 1994), which delays the helium flash. As a result, a heavier inert helium core is formed and the luminosity of the tip of the RG branch (TRGB) increases (e.g. Raffelt, 1996). The NMM may increase A(Li) in RGs because the delayed helium flash may result in activation of the CF mechanism induced by thermohaline mixing

(Sackmann & Boothroyd, 1999; Lattanzio et al., 2015).

The NMM has been constrained using RGs near the TRGB in globular clusters. As I discussed in Section 1.4, the helium core releases the gravitational energy $\epsilon_{\rm grav} \sim 100$ erg g^{-1} s^{-1} near the TRGB. It is therefore concluded that the additional energy loss should not exceed ~ 100 erg g^{-1} s^{-1} to avoid the significant delay of the helium flash. This argument, which does not depend on numerical stellar models, corresponds to an upper limit of $\mu_{12} \lesssim 10$. In order to make tighter constraints, detailed comparison between stellar models and observed RGs has been performed and upper limits $\mu_\nu < 2.2 \times 10^{-12}\mu_{\rm B}$ (Arceo-Díaz et al., 2015) and $\mu_\nu < 1.2 \times 10^{-12}\mu_{\rm B}$ (Capozzi & Raffelt, 2020) are obtained. The most recent work (Capozzi & Raffelt, 2020) improved the conventional limits using a recent distance determination of ω-Centauri by the Gaia DR2 data (Baumgardt et al., 2019). The magnitude of the TRGB is, on the other hand, estimated by applying an edge-filter on the luminosity function of the RG branch (Bellazzini et al., 2001). Considering uncertainties in the TRGB magnitude, extinction, and distance, Capozzi & Raffelt (2020) obtain the TRGB absolute magnitude $M_{\rm I}^{\rm obs} = -3.96 \pm 0.05$ mag in ω-Centauri. On the other hand, the model gives

$$M_{\rm I}^{\rm theory} = -4.08 - \delta M_\mu \pm \sigma_\mu \tag{3.1}$$

where δM_μ is the effect of the NMM and σ_μ is the uncertainty. The fiducial value $M_{\rm I} = -4.08$ is based on Serenelli et al. (2017) and the other terms are given as (Viaux et al., 2013a)

$$\delta M_\mu = 0.23\left(\sqrt{\mu_{12}^2 + 0.80^2} - 0.80 - 0.18\mu_{12}^{1.5}\right) \tag{3.2}$$

$$\sigma_\mu = \sqrt{0.039^2 + (0.046 + 0.0075\mu_{12})^2}. \tag{3.3}$$

Viaux et al. (2013a) consider various possible origins of theoretical uncertainties. In particular, they point out that the largest uncertainty originates from the mixing length and the bolometric correction. Comparing $M_{\rm I}^{\rm theory}$ and $M_{\rm I}^{\rm obs}$ leads to the upper limit $\mu_{12} < 1.2$. Although this limit is very stringent, there are several points to note. The theoretical uncertainty (3.3) is derived to compare their model with the globular cluster M5. Because the age and the metallicity are different, it might be desirable to estimate the uncertainty for ω-Centauri. Also, it is pointed out that $M_{\rm I}^{\rm theory}$ can significantly depend on stellar evolution codes (Serenelli et al., 2017), although Viaux et al. (2013a) do not include the code dependence in their uncertainty.

The aim of this Chapter is to show that a sufficiently large NMM can enhance A(Li) in RC stars and reduce the discrepancy between the observations and the theory. Because it is

ubiquitous physics, the NMM is a candidate to explain the peak in the A(Li) distribution. The rare population with A(Li) > 1.5 is beyond the scope of this study. Section 3.2 describes the stellar models and the treatment of the NMM. Section 3.3 shows the results of my calculations and compares them with the observational data. In Section 3.4, I summarize my results and discuss the future perspective. A part of this Chapter has been submitted to a journal (Mori et al., 2020b).

3.2 Stellar Model

I use Modules for Experiments in Stellar Astrophysics (MESA; Paxton et al., 2011, 2013, 2015, 2018, 2019) version 10398 to construct one-dimensional low-mass stellar models. MESA adopts the equation of state of Rogers & Nayfonov (2002) and Timmes & Swesty (2000) and the opacity of Iglesias & Rogers (1996, 1993) and Ferguson et al. (2005). I adopt nuclear reaction rates compiled by NACRE (Angulo et al., 1999) and Caughlan & Fowler (CF88; 1988). If a reaction rate appears in both, the one tabulated in NACRE is adopted. Notably, the rates for the triple-α reaction and ^{14}N(p, γ)^{15}O are from NACRE and the electron capture rate of ^{7}Be is from CF88. The adopted nuclear reaction network is `pp_extra.net`, which includes ^{1,2}H, ^{3,4}He, ^{7}Li, ^{7}Be, ^{8}B, ^{12}C, ^{14}N, ^{16}O, ^{20}Ne, and ^{24}Mg. Treatment of electron screening is based on Alastuey & Jancovici (1978) and Itoh et al. (1979). The mass loss formula in Reimers (1975) is adopted.

MESA makes use of the mixing length theory (Cox & Giuli, 1968) to calculate the convective luminosity from the temperature gradient. I adopt the Ledoux criterion (Ledoux, 1947) to calculate the convective instability. My model considers thermohaline mixing as well because it affects the lithium abundance (Sackmann & Boothroyd, 1999; Lattanzio et al., 2015). Thermohaline mixing is treated as a diffusive process with the diffusion coefficient (Paxton et al., 2013)

$$D_{\rm thm} = \alpha_{\rm thm} \frac{3K}{2\rho C_{\rm P}} \frac{B}{\nabla_{\rm T} - \nabla_{\rm ad}}, \tag{3.4}$$

where $\alpha_{\rm thm}$ is a free parameter, ρ is the density, $C_{\rm P}$ is the specific heat, B is the Ledoux term (Unno et al., 1989), $\nabla_{\rm T}$ is the actual temperature gradient, and $\nabla_{\rm ad}$ is the adiabatic temperature gradient. K is the thermal conductivity written as

$$K = \frac{4acT^3}{3\kappa\rho}, \tag{3.5}$$

where a is the radiation density constant, c is the speed of light, T is the temperature, and κ is the opacity.

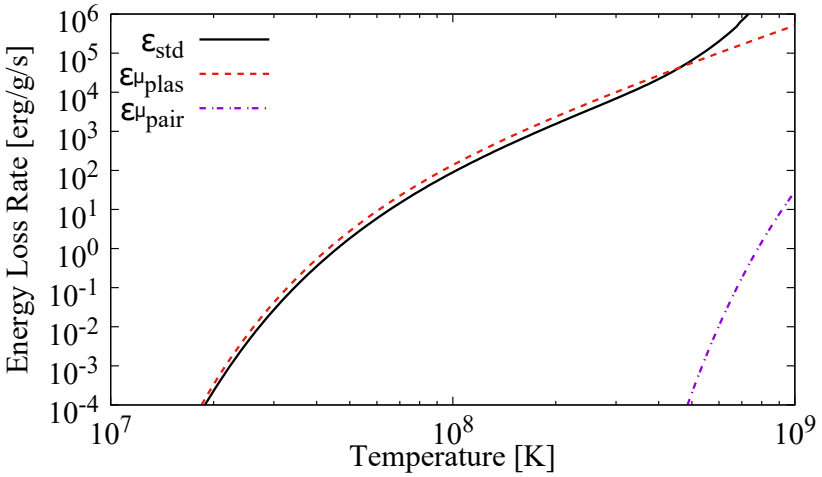

Fig. 3.2 The energy loss rates induced by the neutrino emission with $\mu_\nu = 5 \times 10^{-12}\mu_B$. The density of $\rho = 10^6$ g cm^{-3} is assumed. The black line shows the total standard rate and the other lines show the rates enhanced by the NMM.

The effect of mixing is coupled with the stellar structure as follows. The equation for the mass fraction $X_{i,k}$ of a nucleus i in the k-th cell is (Paxton et al., 2011)

$$X_{i,k}(t+\delta t) - X_{i,k}(t) = dX_{\rm burn} + (F_{i,k+1} - F_{i,k})\frac{\delta t}{dm_k}. \tag{3.6}$$

The first term on the right-hand side represents the change in $X_{i,k}$ due to nuclear burning. The second term counts in the effect of mixing, where dm_k is the mass of the k-th cell and $F_{i,k}$ is defined as

$$F_{i,k} = (X_{i,k} - X_{i,k-1})\frac{\sigma_k}{\overline{dm_k}}. \tag{3.7}$$

where $\sigma_k = D_k(4\pi r^2\rho)^2$ is the Lagrangian diffusion coefficient and $\overline{dm_k} = 0.5(dm_{k-1} + dm_k)$.

The parameters in my models follow those in Kumar et al. (2020). The initial mass is fixed to $1M_\odot$ and the initial metallicity is fixed to be solar: $Z = 0.0148$ (Lodders, 2020). However, the initial lithium abundance in the pre-main sequence is set to $A(\mathrm{Li}) = 2.8$ to fit data. The mixing length is $\alpha = 1.6$ and the thermohaline coefficient is $\alpha_{\rm thm} = 100$ and 50, because A(Li) after the RG branch bump is sensitive to thermohaline mixing.

I consider the plasmon decay and neutrino pair production as the additional energy loss induced by the NMM. The energy loss rates due to the plasmon decay and the the pair production are given by Eqs. (1.10) and (1.12), respectively. Fig. 3.2 shows the energy loss rates with $\mu_\nu = 5 \times 10^{-12}\mu_B$ at $\rho = 10^6$ g cm^{-3}, which is the typical central density at the helium flash. At the temperature of $\sim 10^8$ K, the enhanced energy loss rate is comparable with the standard rate. Also, it is seen that the pair production is negligible in the

$\alpha_{\rm thm}$	μ_{12}	$M_{\rm He,TRGB}/M_\odot$	$\log(L/L_\odot)_{\rm TRGB}$	$A({\rm Li})_{\rm RC}$
100	0	0.467	3.39	−0.90
100	2	0.480	3.46	−0.57
100	3	0.490	3.52	−0.23
100	4	0.500	3.57	0.10
100	5	0.509	3.61	0.38
50	0	0.467	3.39	−0.56
50	2	0.480	3.46	−0.39
50	3	0.490	3.52	−0.16
50	4	0.500	3.57	0.12
50	5	0.509	3.61	0.39

Table. 3.1 The parameters of the models. The zero age main sequence mass and the initial metallicity are fixed to $M_{\rm ZAMS} = 1M_\odot$ and $Z = 0.0148$, respectively. $\alpha_{\rm thm}$ is the thermohaline coefficient, μ_{12} is the NMM, $M_{\rm He,TRGB}$ is the mass of the helium core at the TRGB, $L_{\rm TRGB}$ is the luminosity at the TRGB, and $A({\rm Li})_{\rm RC}$ is the lithium abundance of RC stars. Since A(Li) decreases during the evolution of RC stars, the initial values just after the helium flash are shown.

temperature range of interest.

3.3 Results

3.3.1 Evolution of the Fiducial Model

In this Section, I describe the fiducial model with $\mu_\nu = 0$. Fig. 3.3 shows the evolution of the stellar models in the $L - A$(Li) plane, where L is the luminosity. The solid lines show the evolution of the fiducial model. The upper panel adopts $\alpha_{\rm thm} = 100$ and the lower panel adopts $\alpha_{\rm thm} = 50$. The points are the stellar samples selected by Kumar et al. (2020). The lithium abundances of the samples are estimated by the 6707 Å Li line. It should noted that the data should be biased because lithium cannot be detected when the line is weak.

The evolution starts from a low luminosity (the lower-left side of Fig. 3.3). The lithium abundance A(Li) stays constant during the main sequence. When the star reaches the main-sequence turnoff at $\log(L/L_\odot) = 0.4$, A(Li) starts to decrease from 2.4 to 0.8. This is because surface lithium is conveyed to the stellar interior due to the first dredge-up (Iben, 1967), and is destroyed by the proton capture. The lithium depletion becomes slower as the star evolves, but A(Li) starts to decrease again when the star reaches the RG branch bump at $\log(L/L_\odot) = 1.5$. At this point, the star develops thermohaline mixing between the convective envelope and the hydrogen burning shell (Charbonnel & Zahn, 2007; Lattanzio

et al., 2015). This happens because the mean molecular weight is inverted by ^{3}He(^{3}He, $2p$)^{4}He. Because of thermohaline mixing, lithium in the envelope is conveyed to the inner hot region and destroyed. One can see that A(Li) after the RG branch bump is smaller when a larger $\alpha_{\rm thm}$ is adopted. The decrease of A(Li) stops when $\log(L/L_\odot) = 3.2$ and it starts increasing. This is because thermohaline mixing becomes more effective as the star expands (Lattanzio et al., 2015). The effective mixing helps the CF mechanism work and hence increases A(Li). After the TRGB, the core becomes non-degenerate because of the helium flash and L decreases suddenly. As a result, core helium burning begins and a RC star is formed.

Fig. 3.4 shows the time evolution of A(Li) as a function of the helium core mass $M_{\rm He}$. The behavior of A(Li) is not monotonic. In the fiducial model, thermohaline mixing sets in when $M_{\rm He} \sim 0.25 M_\odot$ and A(Li) starts decreasing because of extra mixing. However, when the core mass reaches $M_{\rm He} \sim 0.42 M_\odot$, A(Li) starts increasing.

In order to understand the evolution of A(Li), I introduce three timescales. I denote the timescale for the electron capture of ^{7}Be as $t_{\rm prod}$, the timescale for ^{7}Li(p, α)^{4}He as $t_{\rm dest}$, and the timescale on which the material at a given radius is conveyed to the bottom of the convective envelope by thermohaline mixing as $t_{\rm mix}$.

Fig. 3.5 shows the profile of the $D_{\rm thm}$, the mixing and nuclear reaction timescales, and the ^{7}Be and ^{7}Li abundances in the region where ^{7}Be is produced. The solid lines indicate the time when $M_{\rm He} = 0.45 M_\odot$ and the broken lines indicate the time when $M_{\rm He} = 0.26 M_\odot$. It is seen that thermohaline mixing becomes more effective as the core grows. This is because the density in this region decreases as a function of time. The lower density leads to a larger K as we can see from Eq. (3.5) and thus a larger $D_{\rm thm}$ (Lattanzio et al., 2015).

This effective mixing below the convective envelope explains why A(Li) decreases after reaching the RG branch bump and increases near the TRGB. ^{7}Be is produced by ^{3}He(α, γ)^{7}Be at $R \sim 10^{-1.3} R_\odot$. In order for the CF mechanism to work, mixing in this region should be efficient enough to convey ^{7}Be to the bottom of the convective envelope. When $M_{\rm He} = 0.26 M_\odot$, ^{7}Be decays into ^{7}Li and is destroyed by the proton capture before being conveyed to the convective envelope, because $t_{\rm mix}$ is much longer than $t_{\rm prod}$ in $R < 10^{-0.2} R_\odot$. Rather, since ^{7}Li in the envelope diffuses into the thermohaline region, A(Li) decreases in time. On the other hand, when $M = 0.45 M_\odot$, $t_{\rm mix}$ becomes shorter than before. As a result, a part of ^{7}Be is conveyed to the envelope before it decays and A(Li) increases.

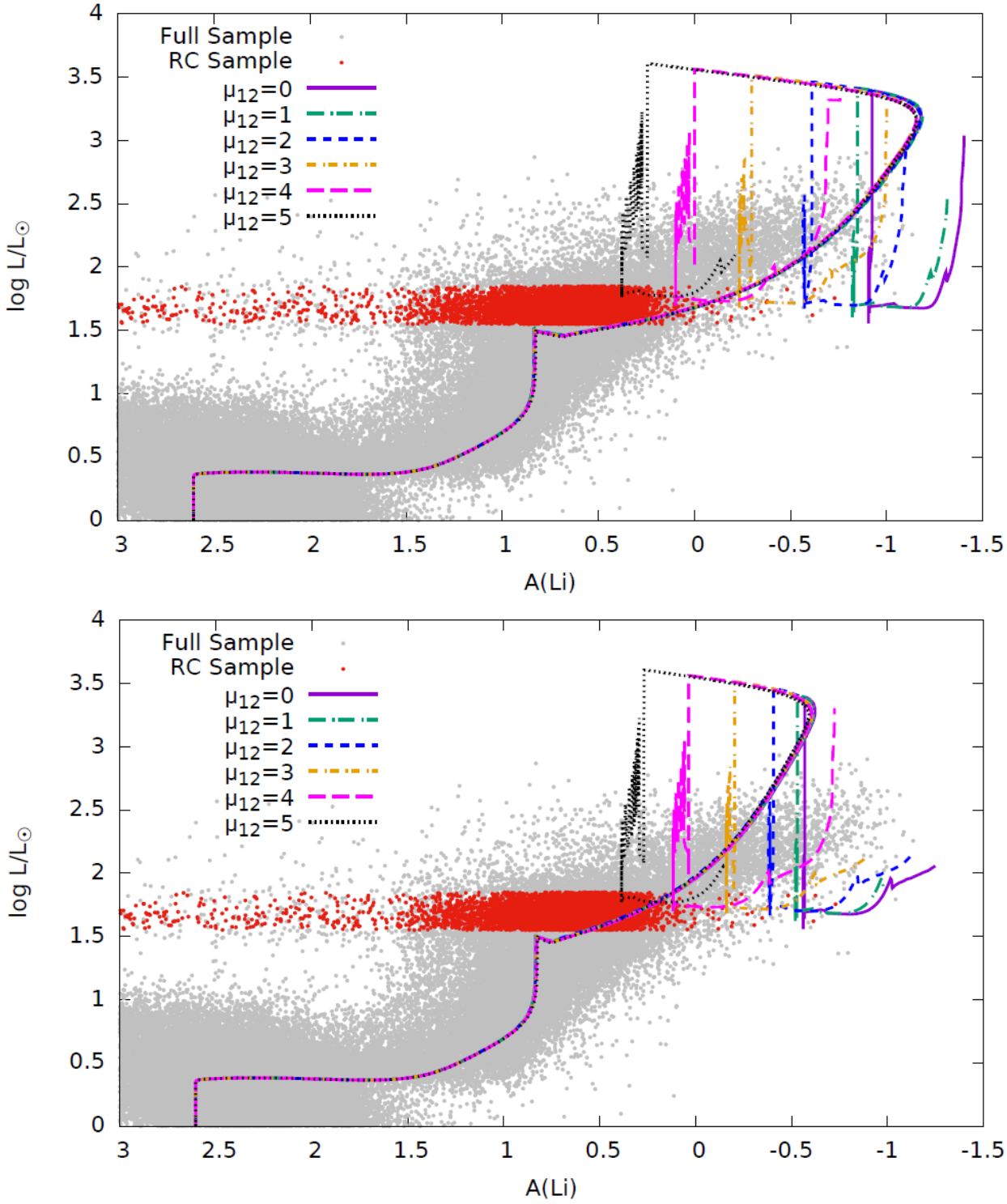

Fig. 3.3 The lines show the evolution of my models with $\mu_{12} = 0 - 5$ in the $L - A(\mathrm{Li})$ plane. The upper panel adopts $\alpha_{\mathrm{thm}} = 100$ and the lower panel adopts $\alpha_{\mathrm{thm}} = 50$. The grey dots are GALAH DR2 samples (Buder et al., 2018) with reliable lithium abundances and the red dots are RC samples selected by Kumar et al. (2020).

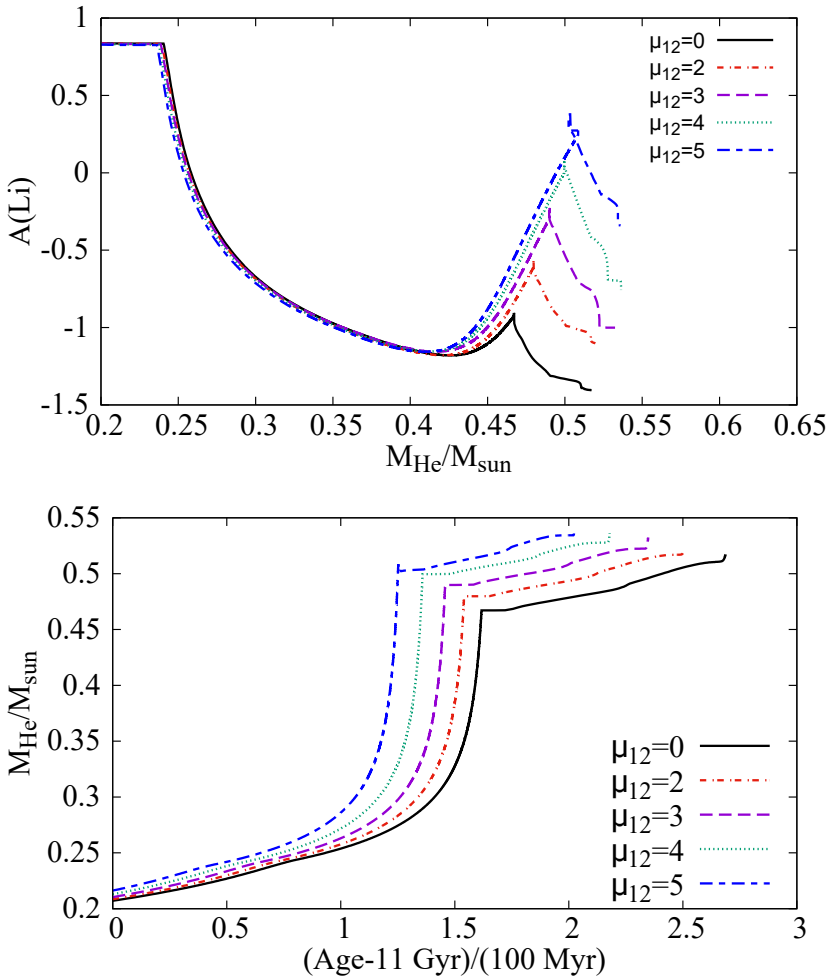

Fig. 3.4 The evolution of the surface lithium abundance as a function of (upper) the helium core mass and (lower) the stellar age. The thermohaline coefficient is fixed to $\alpha_{\rm thm} = 100$.

3.3.2 Dependence on the Neutrino Magnetic Moment

I perform stellar evolution calculations with $\mu_{12} = 1 - 5$, where $\mu_{12} = \mu_\nu/(10^{-12}\mu_{\rm B})$. Even though the higher values of the magnetic moment in this range are ruled out by the constraints from low-mass stars in globular clusters, it is instructive to examine the effect as the magnetic moment values, and hence energy losses, get larger. The adopted parameters and results are summarized in Table 1.

Fig. 3.3 shows the Li abundance evolution for models with $\mu_\nu > 0$, indicated by the broken lines. A(Li) and L at the TRGB increase when a larger value of μ_ν is adopted. The fact that TRGB stars become luminous when μ_ν is adopted has been used to constrain μ_ν (e.g. Raffelt, 1996; Arceo-Díaz et al., 2015; Capozzi & Raffelt, 2020). Fig. 3.4 shows

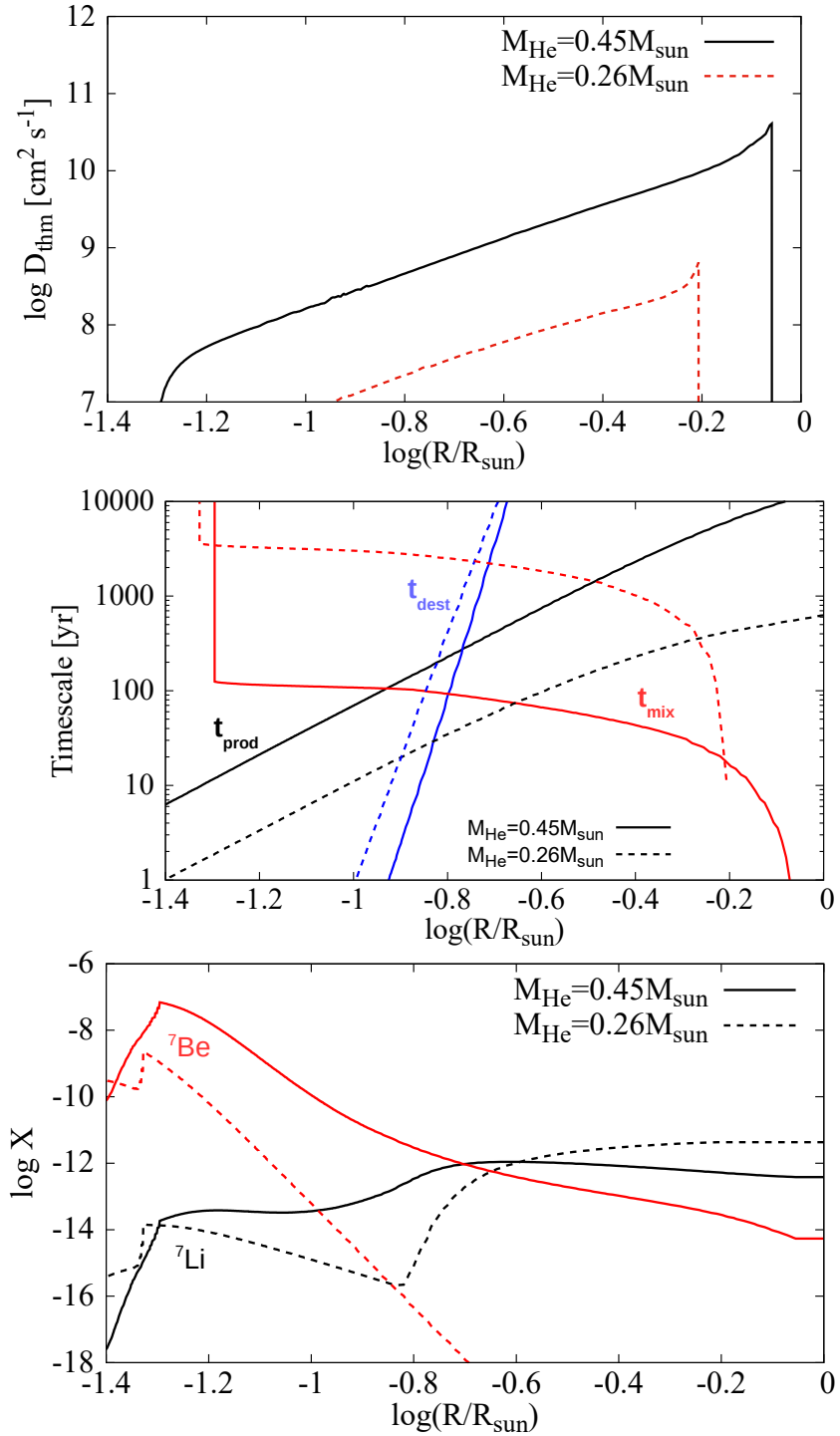

Fig. 3.5 The profile of (upper) $D_{\rm thm}$, (middle) the mixing and nuclear reaction timescales, and (lower) the abundances of ^{7}Be and ^{7}Li. The NMM is not adopted, and $\alpha_{\rm thm} = 100$ is assumed. The solid lines show the model when $M_{\rm He} = 0.45 M_\odot$ and the broken lines show the model when $M_{\rm He} = 0.26 M_\odot$.

$\alpha_{\rm thm}$	μ_{12}	$M_{\rm He,TRGB}/M_\odot$	$\log(L/L_\odot)_{\rm TRGB}$	$A({\rm Li})_{\rm RC}$
100	0	0.467	3.39	−0.90
100	1	0.471	3.41	−0.82
100	2	0.480	3.46	−0.57
100	3	0.490	3.52	−0.23
100	4	0.500	3.57	0.10
100	5	0.509	3.61	0.38
50	0	0.467	3.39	−0.56
50	1	0.471	3.41	−0.52
50	2	0.480	3.46	−0.39
50	3	0.490	3.52	−0.16
50	4	0.500	3.56	0.12
50	5	0.509	3.60	0.39

Table. 3.2 The parameters of the models. The zero age main sequence mass and the initial metallicity are fixed to $M_{\rm ZAMS} = 1M_\odot$ and $Z = 0.0148$, respectively. $\alpha_{\rm thm}$ is the thermohaline coefficient, μ_{12} is the NMM, $M_{\rm He,TRGB}$ is the mass of the helium core at the TRGB, $L_{\rm TRGB}$ is the luminosity at the TRGB, and $A({\rm Li})_{\rm RC}$ is the lithium abundance of RC stars. Since A(Li) decreases during the evolution of RC stars, the initial values just after the helium flash are shown.

the evolution of A(Li) as a function of the helium core mass $M_{\rm He}$ when $\alpha_{\rm thm} = 100$. It is seen that A(Li) decreases when $M_{\rm He}$ exceeds $\sim 0.25M_\odot$ in each model. This is because thermohaline mixing starts being induced by the inversion of the mean molecular weight when $M_{\rm He} \sim 0.25M_\odot$. The peaks around $M_{\rm He} \sim 0.5M_\odot$ correspond to the helium flash. One can confirm that A(Li) at the TRGB is higher when μ_ν is larger.

The physical effects of the lithium enhancement from a non-zero NMM are twofold. One is the formation of a more massive core due to the additional energy loss. Fig. 3.4 shows the time evolution of the core mass. It is seen that the model with $\mu_{12} = 5$ reaches the helium flash ~ 36 Myr earlier than the fiducial model does. Although the models reach the helium flash earlier in time because of the additional energy loss, the helium core at the ignition of central helium burning becomes heavier when the NMM is adopted. This is because central helium burning is ignited when the nuclear energy production exceeds the energy loss rate. If the energy loss rate is larger, the critical temperature for the ignition becomes higher. The more massive core leads to a smaller density above the hydrogen burning shell and hence a larger thermal conductivity (Lattanzio et al., 2015). Since $D_{\rm thm}$ increases as a fuction of conductivity, thermohaline mixing at the TRGB becomes more efficient with a larger NMM. Fig. 3.6 shows the profile of $D_{\rm thm}$ and the mass fractions of ^{7}Be and ^{7}Li at the TRGB. It is seen that $D_{\rm thm}$ is larger if the NMM is larger. Therefore the CF mechanism

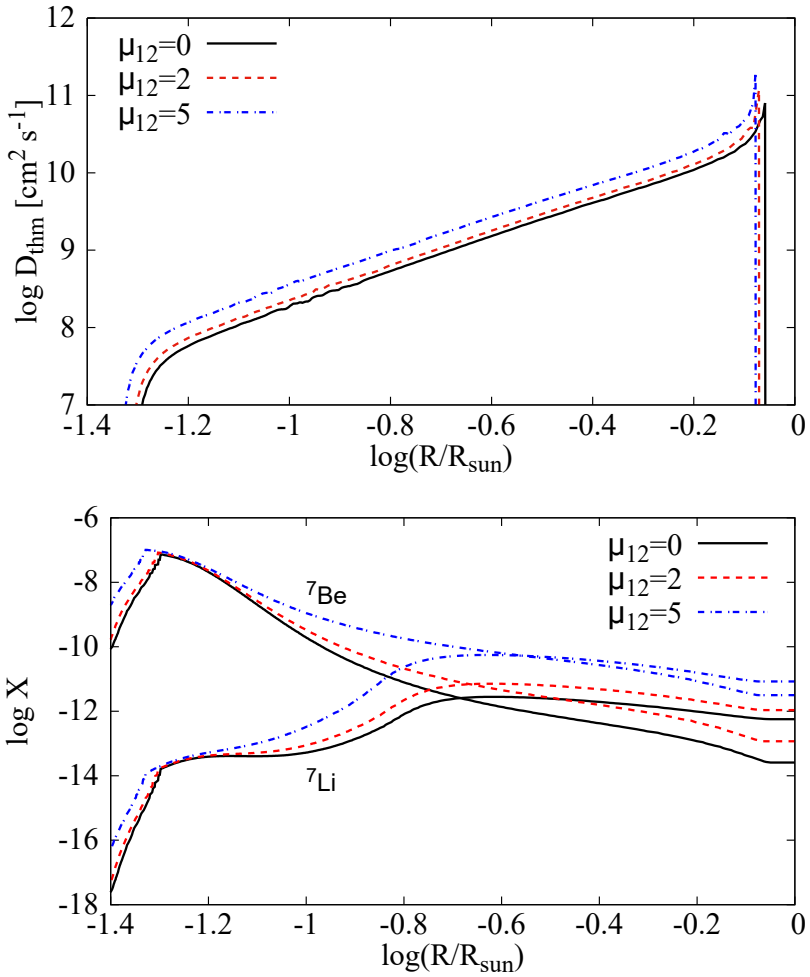

Fig. 3.6 Structure of my model at the TRGB with $\mu_{12} = 0$, 2, and 5. The upper panel shows the thermohaline diffusion coefficient and the lower panel shows the mass fractions of ^{7}Li and ^{7}Be as a function of the radius. The thermohaline coefficient is fixed to $\alpha_{\rm thm} = 100$.

can convey ^{7}Be to the convective envelope more effectively and A(Li) in RC stars becomes higher.

It is seen from Fig. 3.4 that A(Li) starts to deviate from the standard model even before the helium flash. This is explained by changes of stellar structure induced by the NMM. Fig. 3.7 shows the thermohaline diffusion coefficient $D_{\rm thm}$ and the mass fractions of ^{7}Li and ^{7}Be for the models with $\mu_{12} = 0$, 2, and 5 in the region where thermohaline mixing is effective. In this figure, the helium core mass is fixed to $M_{\rm He} = 0.45 M_\odot$. When a larger NMM is adopted, the radius of the helium core becomes smaller and the density in the envelope decreases. The smaller density results in a larger thermal diffusivity and a larger $D_{\rm thm}$ (Lattanzio et al., 2015). Since ^{7}Be produced via ^{3}He(α,γ) is conveyed to the outer region by thermohaline mixing, the more efficient mixing leads to a larger A(Li).

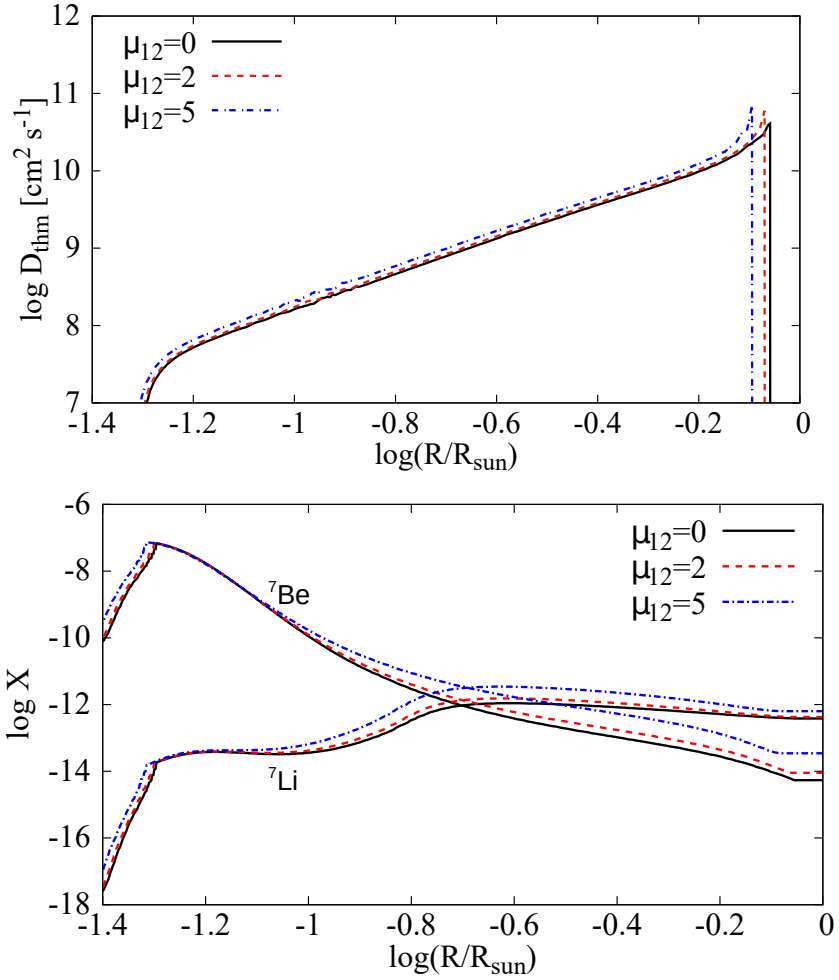

Fig. 3.7 Same as Figure 3.6, but for the time at $M_{\rm He} = 0.45 M_{\odot}$.

Recently, the GALAH (Galactic Archaeology with HERMES) survey second data release (DR2) provided spectroscopic data of 342,682 stars in the Milky Way (Buder et al., 2018). Kumar et al. (2020) selected stars with $\log L/L_{\odot} \in [1.55,\ 1.85]$ and the effective temperature $T_{\rm eff} \in [4650,\ 4900]$ K from the GALAH DR2 samples and identified them as RC stars. Kumar et al. (2020) used GALAH samples that overlap with an astroseismic catalog (Ting, Hawkins & Rix, 2018) to distinguish RC and RG stars. They concluded that the contamination of RGs in their RC samples accounts for only $\sim 10\%$.

Kumar et al. (2020) found that the lithium abundance in RC stars is distributed around $A({\rm Li}) \sim 0.71 \pm 0.39$. This ubiquitous enhancement of lithium has not been predicted by stellar models. When the NMM is not adopted in my model, the lithium abundance in RC stars is only $A({\rm Li}) = -0.90$ (-0.56) when $\alpha_{\rm thm} = 100$ (50). We find that, if $\mu_{12} = 5$ is adopted, $A({\rm Li})$ reaches 0.38 (0.39), which is consistent with the observed $A({\rm Li})$. When $\alpha_{\rm thm}$ is larger, ^{7}Li is destroyed to a greater extent after the RG branch bump and thus $A({\rm Li})$ in

RC stars becomes smaller. Although A(Li) is not sufficiently large when $\mu_{12} = 2-4$ in both cases, the discrepancy in A(Li) becomes smaller if the NMM is adopted. The additional energy loss induced by the NMM is thus a candidate of a ubiquitous mechanism of the high A(Li) in RC stars.

Traditionally, giants with A(Li) > 1.5 have been called lithium-rich giants (Brown et al., 1989). It is difficult to explain such extremely high lithium abundances with the NMM only. Kumar et al. (2020) point out that lithium-rich giants with A(Li) > 1.5 account only for $\sim 3.0\%$ of RC stars. The rare population implies another mechanism which works only in a certain kind of stars.

3.3.3 Dependence on the Initial Lithium Abundance

In the previous Sections, the initial lithium abundance is fixed to A(Li) $= 2.8$. Since a portion of lithium is destroyed during the pre-main sequence, the lithium abundance at the zero-age main sequence is A(Li) $= 2.6$. As we can seen in Fig. 3.3, this value agrees with the observed abundances. However, since the dispersion of the observed abundances is large, it is important to study the effect of the initial lithium abundance.

In order to study the effect of the initial abundance on the abundance evolution in RC stars, I adopt three initial values: A(Li) $= 2.5$, 2.8, and 3.1. Fig. 3.8 shows trajectories in the plane of the luminosity and A(Li) of the models with different initial abundances. The NMM is fixed to $\mu_{12} = 0$ and 5. It is seen that A(Li) in the models with a larger initial abundance stays larger until the star evolves up to $\log L/L_\odot \sim 3.5$, while the difference among the models becomes smaller at and after the helium flash. Especially, A(Li) in RC stars with the different initial abundances becomes indistinguishable in the case of $\mu_{12} = 5$. This is because most of the lithium is produced by the CF mechanism near and after the helium flash. Thus, the contribution of the initial abundance is minor.

3.3.4 Dependence on the Stellar Mass and the Mass Loss

In the previous Sections, the stellar mass is fixed to $1M_\odot$ because the samples in Kumar et al. (2020) have a peak at $1.0M_\odot$. However, the additional energy loss works in stars with a wide range of masses if it exists. In this Section, I investigate the effect of the NMM on $0.9M_\odot$ and $1.2M_\odot$ models as well.

Fig. 3.9 shows L and A(Li) in 0.9, 1.0, and $1.2M_\odot$ models. The NMM is fixed to $\mu_{12} = 0$ and 5. It is seen that a lighter star has a smaller A(Li) in every evolutionary phase. A recent Letter (Schwab, 2020) reported A(Li) in 0.9 and $1.2M_\odot$ models as well. They assume an extra mixing induced by the helium flash and claim that A(Li) in RC stars does not depend

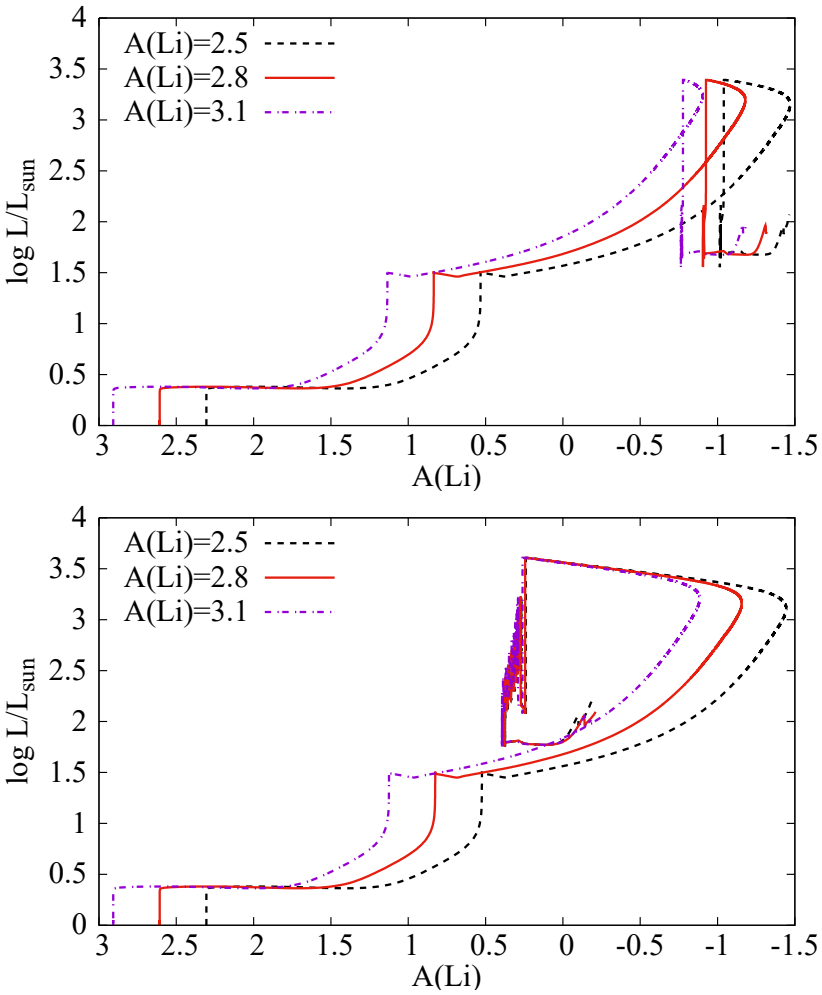

Fig. 3.8 The evolution in the plane of the luminosity and the lithium abundance of the $1M_{\odot}$ models with the initial lithium abundances of A(Li) = 2.5, 2.8, and 3.1. The NMM is fixed to (upper) $\mu_{12} = 0$ and (lower) $\mu_{12} = 5$ and the thermohaline coefficient is fixed to $\alpha_{\rm thm} = 100$.

on the initial mass. Although this difference can be potentially used to distinguish the helium-flash-induced mixing from the enhanced energy loss, further studies are desirable because the evolution of A(Li) depends on input parameters (e.g. α and $\alpha_{\rm thm}$).

The mass loss is another possible origin of uncertainties. In the previous Sections, the scaling factor in Reimers (1975) is fixed to $\eta = 0.3$. I adopt $\eta = 0.1$ and 0.4 to study the effect of mass loss rates on A(Li). Fig. 3.10 shows L and A(Li) in models with different mass loss rates. The different values of η do not lead to significant differences in A(Li) through the evolution. This is because the envelope is convective and thus the chemical composition is uniform.

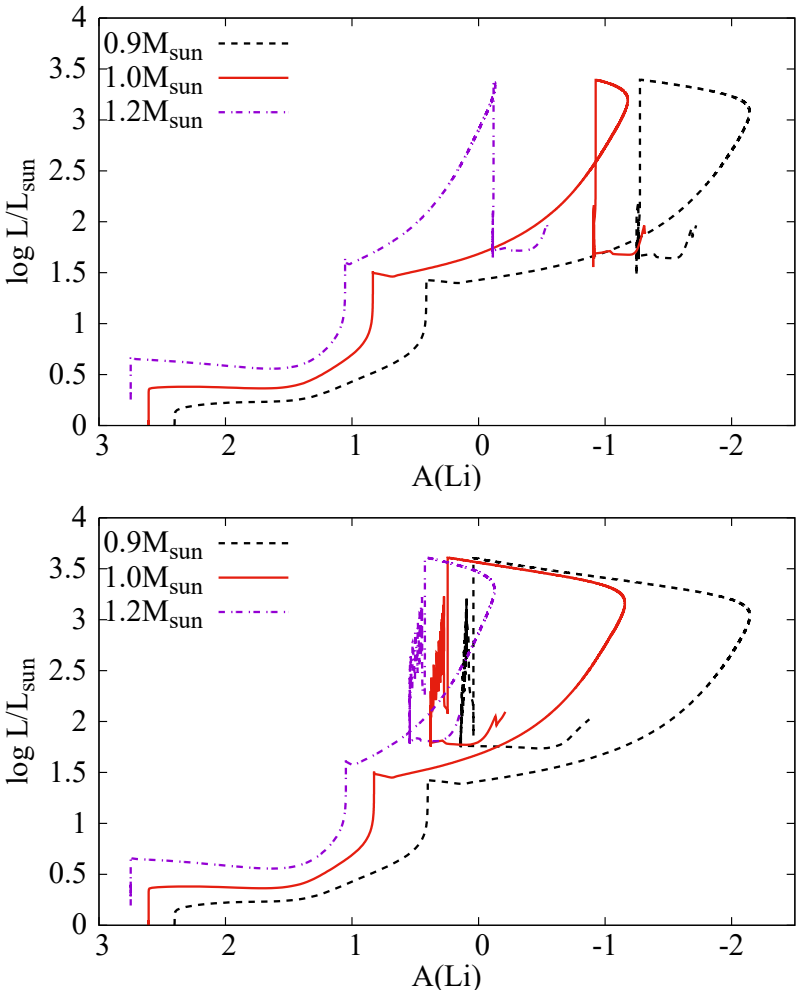

Fig. 3.9 Same as Figure 3.8, but for the $0.9M_{\odot}$, $1.0M_{\odot}$, and $1.2M_{\odot}$ models.

3.3.5 Comparison with Previous Works

The lithium production in RG stars via the CF mechanism has been studied by several works (Lattanzio et al., 2015; Schwab, 2020). They used MESA to produce their stellar models, as I do in this study. In this Section, I compare my models with $\mu_\nu = 0$ with the ones shown in the previous studies.

Lattanzio et al. (2015) studied the effects of numerical treatments on thermohaline mixing in RGs. In order to study differences between stellar evolution codes, they used several codes including MESA. They found that the lithium abundance in RGs depends on the codes and temporal resolution. Their test model adopted the initial mass $1.25M_{\odot}$, the metallicity $Z = 0.0122$ (Asplund, Grevesse & Sauval, 2005), and the initial lithium abundance $A(\mathrm{Li}) = 3.25$. Here I adopt the same parameters and produce a model that mimics

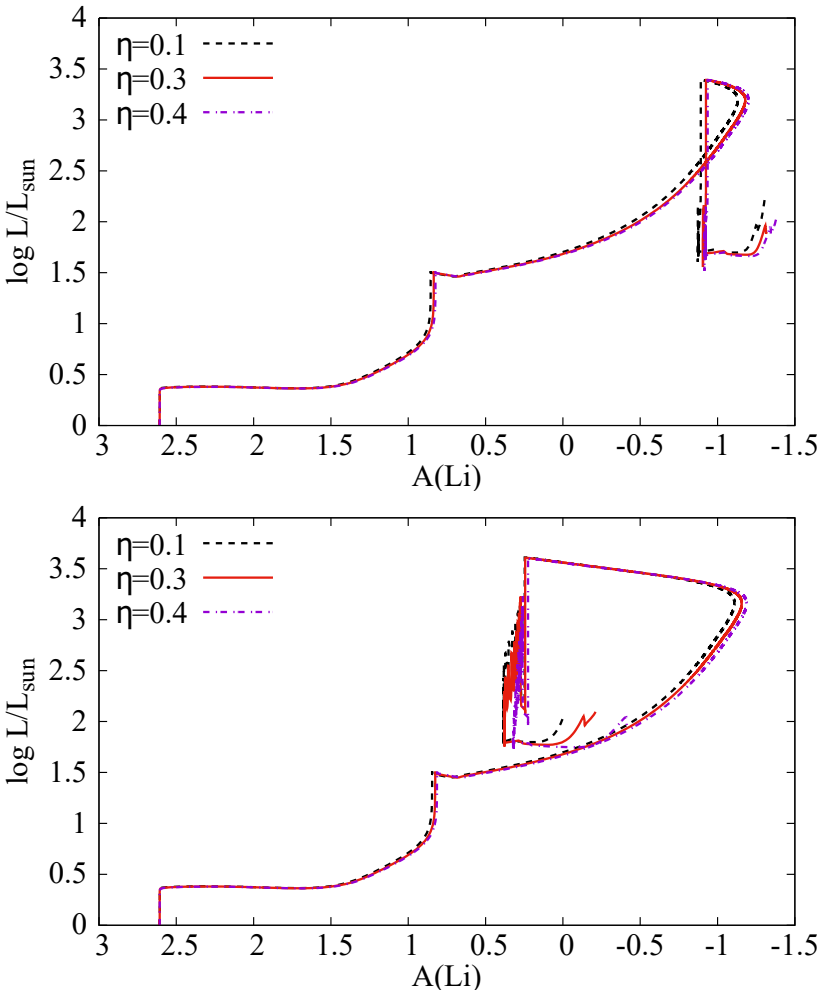

Fig. 3.10 Same as Figure 3.8, but for the mass loss rates of η = 0.1, 0.3, and 0.4.

their model to compare their result with ours. Lattanzio et al. (2015) produced three models with C_t = 100, 1000, and 10000 using MESA, where $C_t = 3\alpha_{thm}/2$. I adopt α_{thm} = 666, which corresponds to C_t = 1000. Table 2 shows the maximum and minimum luminosities $L_{b,max}$ and $L_{b,min}$ in the bump of the RG branch, the luminosity L_{thm} at which A(Li) starts decreasing due to thermohaline mixing, and the lithium abundance $A(\mathrm{Li})_{TRGB}$ at the TRGB in both models. Both models show similar trends. In particular, both show the lithium enhancement near the TRGB. Although the luminosities and A(Li) shown in Table 2 have variations between the models, they are comparable to or even smaller than the variations among the codes (Lattanzio et al., 2015).

Recently, Schwab (2020) studied mixing induced by the helium flash and claimed that it can naturally solve the lithium problem in RC stars proposed by Kumar et al. (2020). They calculated $0.9M_\odot - 2.0M_\odot$ models with and without extra mixing during the helium flash. Their models without extra mixing show smaller values of A(Li) in RC stars when

	$L_{\rm b,max}/L_\odot$	$L_{\rm b,min}/L_\odot$	$L_{\rm thm}/L_\odot$	$A({\rm Li})_{\rm TRGB}$
This work	50	45	48	−0.72
Lattanzio et al. (2015)	47	40	43	−0.85

Table. 3.3 The properties of the $1.25M_\odot$ models in this work and Lattanzio et al. (2015). $L_{\rm b,max}$ and $L_{\rm b,min}$ are the maximum and minimum luminosities in the bump of the RG branch, $L_{\rm thm}$ is the the luminosity at which A(Li) starts decreasing due to thermohaline mixing, and $A({\rm Li})_{\rm TRGB}$ is the lithium abundance at the TRGB.

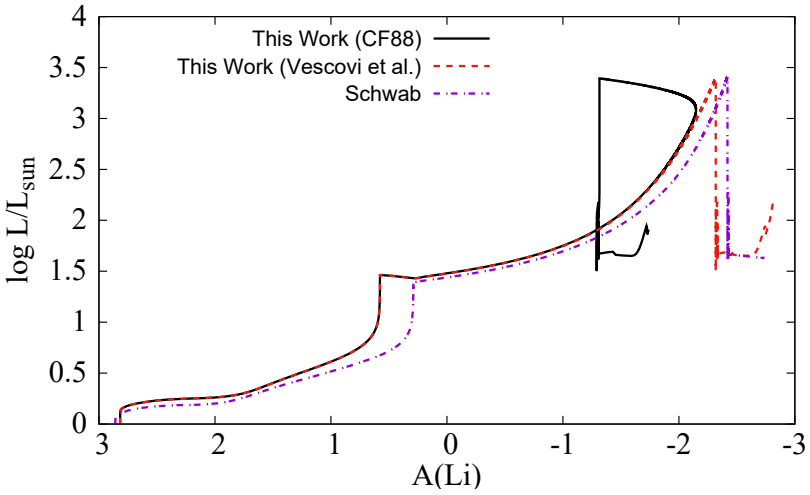

Fig. 3.11 The evolution in the plane of the luminosity and the lithium abundance of the $0.9M_\odot$ models with different ^{7}Be electron capture rates. The black line shows the model that adopts the CF88 rate and the red line shows the model that adopts the rate in Vescovi et al. (2019). The purple line is the model in Schwab (2020) without extra mixing induced by the helium flash.

the stellar mass is smaller. This is consistent with my results shown in Section 3.3.4.

Interestingly, the models in Schwab (2020) do not show the enhancement of lithium near the TRGB in contrast to my models. In order to clarify the origin of the difference, I produce $0.9M_\odot$ models with the mixing length $\alpha = 1.8$, the initial lithium abundance $A({\rm Li}) = 3.26$, and the metallicity $Z = 0.014$ (Asplund et al., 2009). These parameters follow the prescription in Schwab (2020). Fig. 3.11 compares the $0.9M_\odot$ models in Schwab (2020) and this work. Schwab (2020) adopted a recent ^{7}Be electron capture rate calculated by Simonucci et al. (2013) and Vescovi et al. (2019) while I adopted the CF88 rate in the previous Sections. In Fig. 3.11, I use both rates to calculate the models. Fig. 3.11 shows that all models evolve similarly until the luminosity reaches $L \sim 10^3 L_\odot$. However, the lithium abundance starts increasing when I adopt the CF88 rate, while it does not when the other rate is used. Therefore the ^{7}Be electron capture rate has a crucial role in the lithium abundance near the TRGB and in RC stars.

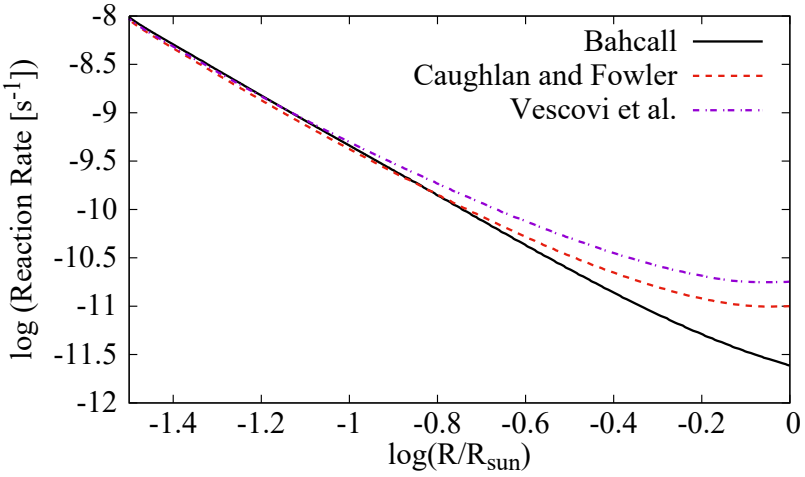

Fig. 3.12 The ^{7}Be electron capture rates as a function of the radius from different works (Bahcall, 1962; Caughlan & Fowler, 1988; Vescovi et al., 2019) in the $1M_\odot$ fiducial model with $\mu_{12} = 0$ and $M_{\rm He} = 0.45M_\odot$. In the previous works, the reaction rates are given as functions of T and ρ. Since T and ρ are given as functions of the radius in my stellar model, the rates are plotted as a function of the radius in this figure.

This behavior can be qualitatively explained as follows. Fig. 3.12 shows the ^{7}Be electron capture rates from different works in the $1M_\odot$ fiducial model with $M_{\rm He} = 0.45M_\odot$. The rate in fully-ionized plasma

$$R = 6.12 \times 10^{-9} \left(\frac{\rho}{\mu T_6^{\frac{1}{2}}} \right) \ {\rm s}^{-1} \tag{3.8}$$

was first derived by Bahcall (1962). Here μ is the mean molecular weight and $T_n = T/(10^n \ {\rm K})$ for an interger n. Later, CF88 proposed a simple analytic formula

$$R = 1.34 \times 10^{-10} \left(\frac{\rho}{\mu T_9^{\frac{1}{2}}} \right) (1 - 0.537 T_9^{\frac{1}{3}} + 3.86 T_9^{\frac{2}{3}} + 0.0027 T_9^{-1} e^{2.515 \times 10^{-3} T_9^{-1}}) \ {\rm s}^{-1} \tag{3.9}$$

which was often used in stellar models. Recently, Simonucci et al. (2013) performed ab-initio calculation beyond the Debye-Hückel approximation of the rate and claimed that it is valid in a wider range of density and temperature. This rate is tabulated in Vescovi et al. (2019). It is seen from Fig. 3.12 that the recent rate (Simonucci et al., 2013; Vescovi et al., 2019) is higher than the traditional rates in the thermohaline region. This means that ^{7}Be decays faster when the recent rate is adopted. If the mixing timescale is fixed, it becomes more difficult to convey ^{7}Be to the envelope before ^{7}Be decays. As a result, A(Li) becomes smaller near the TRGB.

3.4 Discussion

In this Chapter, I discussed the effects of the NMM on A(Li) in RC stars. I found that the production of ^{7}Li near the TRGB is activated when $\mu_{12} = 2 - 5$ is adopted. The ubiquitous high A(Li) in RC stars (Kumar et al., 2020) may be explained by the additional energy loss induced by the NMM.

The destruction and production of ^{7}Li are dependent on deep mixing including thermohaline mixing (Charbonnel & Zahn, 2007; Lattanzio et al., 2015), magnetic buoyancy (Busso et al., 2007), and rotation-induced mixing (Palacios et al., 2003; Charbonnel & Lagarde, 2010; Charbonnel et al., 2020). Fig. 11 in Charbonnel et al. (2020) shows A(Li) in low-mass stellar models with both rotation-induced and thermohaline mixing. The solid lines are non-rotating models and the other lines are rotating models. The lithium abundance stays constant in the non-rotating models while it starts decreasing during the main-sequence in the rotating models. The decrease in A(Li) around $T_{\rm eff} \sim 5500$ K is due to the first dredge-up and the decrease around $T_{\rm eff} \sim 4000$ K is the effect of thermohaline mixing. It is seen that rotation helps the models reproduce the dispersion in the observed samples, although lithium-rich giants are not explained by this model.

The additional energy loss can be induced also by other physics like extra dimensions (Cassisi et al., 2000) and axion-like particles (Raffelt & Dearborn, 1987; Ayala et al., 2014). Since they are expected to result in the similar enhancement of A(Li), they can be a candidate of the mechanism of the lithium enhancement as well.

The enhancement of energy loss rate from neutrino emission affects Li abundances on stellar surfaces through a change in stellar structure, including He core mass and total mass, and its evolution time scale. This characterizes the current theoretical prediction distinguished from other possibilities. For example, in addition to the ^{7}Be production via the ^{3}He(α,γ) reaction operating deep inside the stars, stellar surfaces can be polluted from outside by accretion of companion stellar ejecta or nucleosynthesis via flare-accelerated nuclei on stellar surfaces. If the observed high abundances of Li originate from nucleosynthesis in companion asymptotic giant branch stars (Ventura & D'Antona, 2010), observed stars can have enhanced abundances of carbon and s-nuclei. On the other hand, if nuclear reactions of flare-accelerated nuclei (Tatischeff & Thibaud, 2007) are providing ^{6,7}Li, the isotopic fraction of ^{6}Li is expected to be high. Furthermore, the observed Li-rich stars must be associated with very strong flare activities and simultaneous production of Be and B. In this way, respective possibilities are associated with different astronomical observables to be measured in future.

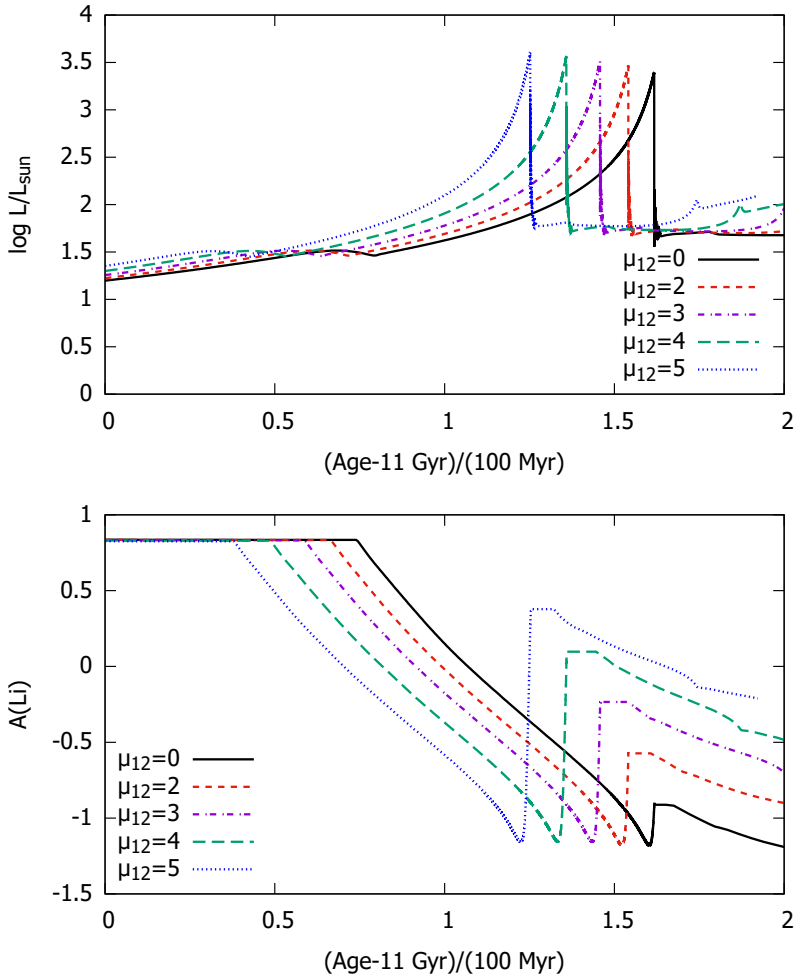

Fig. 3.13 The time evolution of L and A(Li) in the models with $\alpha_{\rm thm} = 100$. The solid line shows the model without the NMM and the other lines show the models with finite values of the NMM.

In principle, it is possible to test my scenario with astronomical observations. Fig. 3.13 shows L and A(Li) of stars near the TRGB as a function of time. It is seen that RGs become luminous rapidly as they evolve toward the TRGB. When a finite NMM is adopted, A(Li) is abruptly enhanced just before the helium flash. The model with $\mu_{12} = 5$ predicts that A(Li) starts increasing $\sim$ 3 Myr before the helium flash. Although such stars are rare, exploring the lithium abundance in the most luminous RGs would be interesting.

Chapter 4

Summary and Future Prospect

In this thesis, I investigated the effects of the NMM and the LEDs on low- and intermediate-mass stars. The additional energy loss induced by them affects the stellar structure and evolution and leads to observable signatures. These concepts were introduced in Chapter 1. I implemented the additional energy loss in a stellar evolution code.

In Chapter 2, I discussed the evolution of intermediate-mass stars which form the blue loops in the HR diagram during their central helium burning. I found that the blue loops are eliminated because of the additional energy loss. Since stars in the instability strip are observed as Cepheid variables, the elimination of the loops can be used to constrain the NMM. It is concluded that μ_ν should be smaller than $\sim (2 \times 10^{-10} - 4 \times 10^{-11})\mu_{\rm B}$ and the fundamental scale in the (4+2)-spacetime should be larger than $\sim 2 - 5$ TeV, depending on the $^{12}{\rm C}(\alpha,\ \gamma)^{16}{\rm O}$ reaction rates and the metallicity.

In Chapter 3, I calculated the surface lithium abundance in low-mass stars. While ^{7}Li is destroyed by the proton capture reaction when it is conveyed to the hot inner region, ^{7}Li is produced via the Cameron-Fowler mechanism near the TRGB when thermohaline mixing is taken into account. I found that the lithium production becomes more active if the NMM of $(2 - 5) \times 10^{-12}\mu_{\rm B}$ is considered because thermohaline mixing becomes more efficient and a heavier helium core is formed. This study is motivated by a recent work (Kumar et al., 2020) which discovered that all of RC stars have high lithium abundances that had not been predicted by stellar models. My result shows that the additional energy loss induced by physics beyond the SM can mitigate the lithium problem in low-mass stars.

In this thesis, I focused on the energy loss induced by the NMM and LED. However, similar effects can be induced by other processes too. Especially, the XENON1T experiment reported excess electronic recoil events that can be interpreted as a signature of Solar axions (Aprile et al., 2020). Although contamination of tritium is not excluded, this experimental result motivates astrophysical studies on the effect of axions on stars.

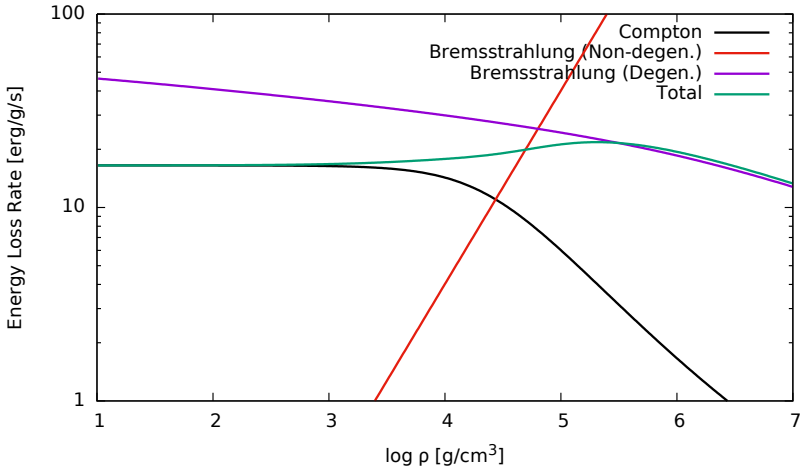

Fig. 4.1 The energy loss rate induced by axions. The temperature is fixed to 10^8 K and the axion-electron coupling constant is fixed to 3.5×10^{-13}. The prescription derived by Raffelt & Weiss (1995) is adopted.

Axions couple with electrons and photons and induce an energy loss in stellar plasma. Fig. 4.1 shows the axionic energy loss rate at $T = 10^8$ K. It is desirable to study the impact of the energy loss in the future. Also, the Li production in low-mass RGs is highly dependent on nuclear physics like ^{7}Be electron capture rates as Fig. 3.11 shows. Thorough understanding of the interplay among stellar macrophysics, nuclear reactions, and exotic physics is desirable to explore possible mechanisms of the Li enhancement.

Appendix A

Plasmon Decay

In stellar plasma, photons acquire an effective mass because of the interaction with electrons. As a result, a quasiparticle called plasmons is excited. If the mass of a neutrino pair is sufficiently small, plasmons can decay into neutrino-antineutrino pairs as Fig 1.3 shows. The plasmon decay is a major channel for the energy loss from stars. In this Appendix, the plasmon decay rates are briefly reviewed on the basis of Haft, Raffelt & Weiss (1994).

The dispersion relation of plasmons is written as

$$\omega^2 - k^2 = \pi_s(\omega,\ k), \tag{A.1}$$

where ω is the frequency and k is the magnitude of the three-dimensional wave number. The subscript $s = \mathrm{T}$ or L stands for the transverse and longitudinal plasmons, respectively. The solution of the dispersion is written as $\omega_{s,k}$. The right hand side of Eq. (A.1) is written as (Braaten & Segel, 1993)

$$\pi_{\mathrm{T}}(\omega,\ k) = \omega_{\mathrm{P}}^2\left(1 + \frac{1}{2}G\left(\frac{v_*^2k^2}{\omega^2}\right)\right), \tag{A.2}$$

$$\pi_{\mathrm{L}}(\omega,\ k) = \omega_{\mathrm{P}}^2\left(1 - G\left(\frac{v_*^2k^2}{\omega^2}\right)\right) + v_*^2k^2 - k^2, \tag{A.3}$$

where ω_{P} is the plasma frequency and $v_* = \omega_1/\omega_{\mathrm{P}}$. The frequencies are defined as

$$\omega_{\mathrm{P}}^2 = \frac{4\alpha}{\pi}\int_0^\infty dp\left(v - \frac{1}{3}v^3\right)pf(E_p), \tag{A.4}$$

$$\omega_1^2 = \frac{4\alpha}{\pi}\int_0^\infty dp\left(\frac{5}{3}v^3 - v^5\right)pf(E_p), \tag{A.5}$$

where $v = p/E_p$ and $f(E)$ is the distribution function. The function $G(x)$ is defined by

$$G(x) = 6\sum_{n=1}^{\infty}\frac{x^n}{(2n+1)(2n+3)}. \tag{A.6}$$

Eqs. (A.2) and (A.3) are exact to $O(\alpha)$. I define the renormalization constant

$$Z_{s,k} = \left(1 - \frac{\partial \pi_s(\omega,\ k)}{\partial \omega^2}\bigg|_{\omega=\omega_{s,k}}\right)^{-1}. \tag{A.7}$$

Z_s is explicitly written as

$$Z_{\mathrm{T},k} = \frac{2\omega_{\mathrm{T},k}^2(\omega_{\mathrm{T},k}^2 - v_*^2k^2)}{\omega_{\mathrm{T},k}^2(3\omega_{\mathrm{P}}^2 - 2\pi_{\mathrm{T}}(\omega_{\mathrm{T},k},\ k)) + (\omega_{\mathrm{T},k}^2 + k^2)(\omega_{\mathrm{T},k}^2 - v_*^2k^2)}, \tag{A.8}$$

$$Z_{\mathrm{L},k} = \frac{2\omega_{\mathrm{L},k}^2(\omega_{\mathrm{L},k}^2 - v_*^2k^2)}{(3\omega_{\mathrm{P}}^2 - (\omega_{\mathrm{L},k}^2 - v_*^2k^2))\pi_{\mathrm{L}}(\omega_{\mathrm{L},k},\ k)}. \tag{A.9}$$

Evaluation of the Feynman diagrams leads to the plasmon decay widths. In the Standard Model, the width is (Adams et al., 1963; Zaidi, 1965)

$$\Gamma_{s,k} = \frac{C_{\mathrm{V}}^2 G_{\mathrm{F}}^2}{48\pi^2\alpha}\frac{Z_{s,k}\pi_s(\omega_{s,k},\ k)^3}{\omega_{s,k}}, \tag{A.10}$$

where G_{F} is the Fermi coupling constant and

$$C_{\mathrm{V}}^2 = \left(\frac{1}{2} + 2\sin^2\theta_{\mathrm{W}}\right)^2 + 2\left(\frac{1}{2} - 2\sin^2\theta_{\mathrm{W}}^2\right)^2 \approx 0.9325 \tag{A.11}$$

is the effective vector coupling constant. Here θ_{W} is the Weinberg angle. On the other hand, the plasmon decay induced by the NMM is given by

$$\Gamma_{s,k}^{\mu} = \frac{\mu_\nu^2}{24\pi}\frac{Z_{s,k}\pi_s(\omega_{s,k},\ k)^2}{\omega_{s,k}}. \tag{A.12}$$

Once $\Gamma_{s,k}$ is given, the energy loss rate per unit volume is calculated by

$$Q_{\mathrm{T}} = 2\int_0^\infty \frac{dk\ k^2}{2\pi^2}\frac{\Gamma_{\mathrm{T},k}\omega_{\mathrm{T},k}}{e^{\frac{\omega_{\mathrm{T},k}}{T}} - 1}, \tag{A.13}$$

$$Q_{\mathrm{L}} = \int_0^{k_{\max}} \frac{dk\ k^2}{2\pi^2}\frac{\Gamma_{\mathrm{L},k}\omega_{\mathrm{L},k}}{e^{\frac{\omega_{\mathrm{L},k}}{T}} - 1}. \tag{A.14}$$

The factor 2 in Q_{T} stands for the two degrees of freedom of the transverse mode. Because the plasmon decay is possible only if the plasmon four-momentum is timelike, the longitudinal mode should satisfy the condition

$$k < k_{\max} = \omega_{\mathrm{P}}\left(\frac{3}{v_*^2}\left(\frac{1}{2v_*}\log\left(\frac{1+v_*}{1-v_*}\right) - 1\right)\right)^{\frac{1}{2}}. \tag{A.15}$$

Inserting Eqs. (A.10) and (A.12) into Eqs. (A.13) and (A.14) gives the energy loss rates for the standard coupling and NMM:

$$Q_{\rm plas} = \frac{C_{\rm V}^2 G_{\rm F}^2}{96\pi^4\alpha} T^3 \omega_{\rm P}^6 Q_3, \tag{A.16}$$

$$Q_{\rm plas}^{\mu} = \frac{\mu_\nu^2}{48\pi^3} T^3 \omega_{\rm P}^4 Q_2. \tag{A.17}$$

Here $Q_n = Q_n^{\rm T} + Q_n^{\rm L}$ $(n = 2,\ 3)$ is defined as

$$Q_n^{\rm T} = 2\int_0^{\infty} \frac{dk\ k^2}{T^3} Z_{{\rm T},k} \left(\frac{\pi_{\rm T}(\omega_{{\rm T},k}, k)}{\omega_{\rm P}^2}\right)^n \frac{1}{e^{\frac{\omega_{{\rm T},k}}{T}} - 1}, \tag{A.18}$$

$$Q_n^{\rm L} = \int_0^{k_{\rm max}} \frac{dk\ k^2}{T^3} Z_{{\rm L},k} \left(\frac{\pi_{\rm L}(\omega_{{\rm L},k}, k)}{\omega_{\rm P}^2}\right)^n \frac{1}{e^{\frac{\omega_{{\rm L},k}}{T}} - 1}. \tag{A.19}$$

The ratio between the standard decay rate and the one with NMM is given as

$$\frac{\epsilon_{\rm plas}^{\mu}}{\epsilon_{\rm plas}} = \frac{2\pi\alpha\mu_\nu^2}{C_{\rm V}^2 G_{\rm F}^2 \omega_{\rm P}^2} \frac{Q_2}{Q_3} = 0.318\mu_{12}^2 \left(\frac{10\ {\rm keV}}{\omega_{\rm P}}\right)^2 \frac{Q_2}{Q_3}. \tag{A.20}$$

Haft, Raffelt & Weiss (1994) numerically evaluated the ratio Q_2/Q_3 and found that its value is $O(1)$. This factor is hence replaced by unity in Eq. (1.10).

Appendix B

Pair Production

When the temperature T in stellar plasma is higher than ~ 0.5 GK, the contribution of the neutrino pair production to the energy loss rate becomes significant (Fig. **??**). In this Appendix, I discuss the pair production induced by NMM on the basis of Heger et al. (2009).

The pair production is represented by the diagram shown in the right panel of Fig. 1.3. The four-momentum of electrons and positrons is denoted by $p_i = (E_i, \mathbf{p}_i)$ and that of neutrinos and antineutrinos is denoted by $q_i = (\omega_i, \mathbf{q}_i)$. The energy loss rate per unit volume is defined as

$$Q_{\rm pair} = \frac{4}{(2\pi)^6}\int \frac{d^3p_1}{e^{\frac{E_1-\mu}{T}}+1}\frac{d^3p_2}{e^{\frac{E_2+\mu}{T}}+1}(E_1+E_2)v_{\rm rel}\sigma_{\rm pair}, \tag{B.1}$$

where μ is the chemical potential, $v_{\rm rel}$ is the relative velocity, and $\sigma_{\rm pair}$ is the spin-averaged cross section. The factor $E_1E_2v_{\rm rel}\sigma_{\rm pair}$ is written as

$$E_1E_2v_{\rm rel}\sigma_{\rm pair} = \frac{1}{4}\int \frac{d^3q_1d^3q_2}{(2\pi)^3 2\omega_1 (2\pi)^3 2\omega_2}|M|^2(2\pi)^4\delta^{(4)}(p_1+p_2-q_1-q_2), \tag{B.2}$$

where $|M|^2$ is the spin-averaged amplitude. Using the Mandelstam variables s, t, and u (Mandelstam, 1958), $|M|^2$ is written as

$$|M|^2 = \frac{e^2\mu_\nu^2}{s}(s^2-(u-t)^2). \tag{B.3}$$

The integration is then evaluated as

$$E_1E_2v_{\rm rel}\sigma_{\rm pair} = \frac{\alpha\mu_\nu^2}{12}(s+2m_e^2), \tag{B.4}$$

where m_e is the electron mass. Putting this result into Eq. (B.1) results in

$$Q_{\rm plas} = \frac{\alpha\mu_\nu^2}{6\pi^4}\int_{m_e}^{\infty}dE_1\int_{m_e}^{\infty}dE_2p_1p_2\frac{(E_1+E_2)(E_1E_2+2m_e^2)}{(e^{\frac{E_1-\mu}{T}}+1)(e^{\frac{E_2+\mu}{T}}+1)}. \tag{B.5}$$

If the dimensionless parameters $\lambda = T/m_e$ and $\nu = \mu/T$ are introduced, $Q_{\rm pair}$ can be written as

$$Q_{\rm pair} = \frac{\alpha\mu_\nu^2 m_e^7}{6\pi^4}(2G^-_{-\frac{1}{2}}G^+_0 + 2G^-_0 G^+_{-\frac{1}{2}} + G^-_0 G^+_{\frac{1}{2}} + G^-_{\frac{1}{2}}G^+_0), \tag{B.6}$$

where the function $G^\pm_n(\lambda,\ \nu)$ is defined by

$$G^\pm_n(\lambda,\ \nu) = \lambda^{3+2n}\int_{\lambda^{-1}}^{\infty} dx \frac{x^{2n+1}(x^2-\lambda^{-2})^{\frac{1}{2}}}{e^{x\pm\nu}+1}. \tag{B.7}$$

This formula cannot be evaluated analytically. However, Heger et al. (2009) suggested that the energy loss rate per unit mass is approximated by a simple formula (1.12) when the pair production is the dominant process.

The Standard Model gives the pair production rate of (Dicus, 1972)

$$\begin{aligned} Q_{\rm pair} = \frac{G_{\rm F}^2 m_e^9}{18\pi^5}((7C_{\rm V}^2 - 2C_{\rm A}^2)(G^-_0 G^+_{-\frac{1}{2}} + G^-_{-\frac{1}{2}}G^+_0) + 9C_{\rm V}^2(G^-_{\frac{1}{2}}G^+_0 + G^-_0 G^+_{\frac{1}{2}}) + \\ (C_{\rm V}^2 + C_{\rm A}^2)(4G^-_1 G^+_{\frac{1}{2}} + 4G^-_{\frac{1}{2}}G^+_1 - G^-_1 G^+_{-\frac{1}{2}} - G^-_{\frac{1}{2}}G^+_0 - G^-_0 G^+_{\frac{1}{2}} - G^-_{-\frac{1}{2}}G^+_1)), \end{aligned} \tag{B.8}$$

where $C_{\rm V} = 1/2 + 2\sin^2\theta_{\rm W}$ and $C_{\rm A} = 1/2$. Fig. **??** shows the energy loss rates with the standard interaction and NMM of $\mu_{12} = 200$. It is seen that the pair production is a dominant neutrino emission process at $T > 0.5$ GK. However, the non-standard pair production rate $\epsilon^\mu_{\rm plas}$ is smaller than the standard rate $\epsilon_{\rm plas}$. This shows that $\epsilon^\mu_{\rm plas}$ is not important if NMM is in the range of interest (i.e. $\mu_{12} < O(100)$).

Appendix C

MESA Inlists

Files that define the configuration of calculations in MESA are called inlists. In this Appendix, MESA inlists used in this study are shown to help readers reproduce the results described in this thesis.

C.1 The inlist used in Chapter 2

```
&star_job

      show_log_description_at_start = .false.
      save_model_when_terminate = .true.
      save_model_filename = 'final.mod'
      change_initial_net = .true.
      new_net_name = 'approx21_plus_co56.net'
      pgstar_flag = .false.
      kappa_file_prefix = 'gs98'

! end of star_job namelist


&controls

      use_gold_tolerances = .true.
      smooth_convective_bdy = .true.
      convective_bdy_weight = 1
      use_other_neu = .true.
      initial_mass = 10
      initial_z = 2d-2

      photo_interval = 50
      profile_interval = 50
      history_interval = 1
      terminal_interval = 1
      write_header_frequency = 10
```

```
num_trace_history_values = 0
trace_history_value_name(1) = 'power_neutrinos'

xa_central_lower_limit_species(1) = 'he4'
xa_central_lower_limit(1) = 1d-8

prune_bad_cz_min_Hp_height = 0
remove_mixing_glitches = .true.

clip_D_limit = 0
okay_to_remove_mixing_singleton = .true.

min_convective_gap = -1

min_thermohaline_gap = 0

min_thermohaline_dropout = 0
max_dropout_gradL_sub_grada = 1d-3
min_semiconvection_gap = 0
remove_embedded_semiconvection = .false.

mesh_delta_coeff = 1
cool_wind_RGB_scheme = 'Dutch'
cool_wind_AGB_scheme = 'Dutch'
RGB_to_AGB_wind_switch = 1d-4
Dutch_scaling_factor = 0.8

log_center_density_limit = 12
log_center_temp_limit = 10.3d0

xa_scale = 1d-5
newton_itermin = 2

mixing_length_alpha = 1.6
max_num_profile_models = 10000
min_timestep_limit = -1
delta_lgL_He_limit = -1

dX_nuc_drop_max_A_limit = -1
dX_nuc_drop_min_X_limit = 1d-4
dX_nuc_drop_limit = 5d-3
dX_nuc_drop_hard_limit = 1d99

delta_lgTeff_limit = 0.005
delta_lgL_limit = 0.05
delta_lgRho_cntr_limit = 0.02

max_allowed_nz = 80000

mesh_dlog_pp_dlogP_extra = 0.15
```

```
mesh_dlog_cno_dlogP_extra = 0.15

mesh_dlog_3alf_dlogP_extra = 0.15
mesh_dlog_burn_c_dlogP_extra = 0.15

mesh_dlog_burn_n_dlogP_extra = 0.15
mesh_dlog_burn_o_dlogP_extra = 0.15

mesh_dlog_burn_ne_dlogP_extra = 0.15

mesh_dlog_burn_na_dlogP_extra = 0.15
mesh_dlog_burn_mg_dlogP_extra = 0.15

mesh_dlog_cc_dlogP_extra = 0.15
mesh_dlog_co_dlogP_extra = 0.15

mesh_dlog_oo_dlogP_extra = 0.15

mesh_dlog_burn_si_dlogP_extra = 0.15
mesh_dlog_burn_s_dlogP_extra = 0.15
mesh_dlog_burn_ar_dlogP_extra = 0.15
mesh_dlog_burn_ca_dlogP_extra = 0.15
mesh_dlog_burn_ti_dlogP_extra = 0.15
mesh_dlog_burn_cr_dlogP_extra = 0.15
mesh_dlog_burn_fe_dlogP_extra = 0.15

mesh_dlog_pnhe4_dlogP_extra = 0.15
mesh_dlog_other_dlogP_extra = 0.15
mesh_dlog_photo_dlogP_extra = 1

overshoot_f_above_nonburn_core = 0.01
overshoot_f_above_nonburn_shell = 0.01
overshoot_f_below_nonburn_shell = 0.01
overshoot_f_above_burn_h_core = 0.01
overshoot_f_above_burn_h_shell = 0.01
overshoot_f_below_burn_h_shell = 0.01

overshoot_f0_above_nonburn_core = 0.005
overshoot_f0_above_nonburn_shell = 0.005
overshoot_f0_below_nonburn_shell = 0.005
overshoot_f0_above_burn_h_core = 0.005
overshoot_f0_above_burn_h_shell = 0.005
overshoot_f0_below_burn_h_shell = 0.005

mesh_dlog_pp_dlogP_extra = 0.15
mesh_dlog_cno_dlogP_extra = 0.15

mesh_dlog_3alf_dlogP_extra = 0.15
mesh_dlog_burn_c_dlogP_extra = 0.15
```

```
      mesh_dlog_burn_n_dlogP_extra = 0.15
      mesh_dlog_burn_o_dlogP_extra = 0.15

      mesh_dlog_burn_ne_dlogP_extra = 0.15

      mesh_dlog_burn_na_dlogP_extra = 0.15
      mesh_dlog_burn_mg_dlogP_extra = 0.15

      mesh_dlog_cc_dlogP_extra = 0.15
      mesh_dlog_co_dlogP_extra = 0.15

      mesh_dlog_oo_dlogP_extra = 0.15

      mesh_dlog_burn_si_dlogP_extra = 0.15
      mesh_dlog_burn_s_dlogP_extra = 0.15
      mesh_dlog_burn_ar_dlogP_extra = 0.15
      mesh_dlog_burn_ca_dlogP_extra = 0.15
      mesh_dlog_burn_ti_dlogP_extra = 0.15
      mesh_dlog_burn_cr_dlogP_extra = 0.15
      mesh_dlog_burn_fe_dlogP_extra = 0.15

      mesh_dlog_pnhe4_dlogP_extra = 0.15
      mesh_dlog_other_dlogP_extra = 0.15
      mesh_dlog_photo_dlogP_extra = 1

      xa_function_species(1) = 'ne20'
      xa_function_weight(1) = 20
      xa_function_param(1) = 1d-2

      xa_function_species(1) = 'si28'
      xa_function_weight(1) = 20
      xa_function_param(1) = 1d-2

      xa_function_species(1) = 's32'
      xa_function_weight(1) = 20
      xa_function_param(1) = 1d-2

      xa_function_species(1) = 'fe54'
      xa_function_weight(1) = 20
      xa_function_param(1) = 1d-2

      xa_function_species(1) = 'fe56'
      xa_function_weight(1) = 20
      xa_function_param(1) = 1d-2

      min_overshoot_q = 1d-3
      T_mix_limit = 1d4

/ ! end of controls namelist
```

C.2 The inlist used in Chapter 3

```
&star_job

      show_log_description_at_start = .false.
      create_pre_main_sequence_model = .true.
      save_model_when_terminate = .true.
      save_model_filename = 'final.mod'
      kappa_file_prefix = 'gs98'
      change_initial_net = .true.
      new_net_name = 'pp_extras.net'
      history_columns_file = 'history_columns_KM.list'

      pre_ms_relax_num_steps = 50

      set_abundance = .true.
      set_initial_abundance = .true.
      chem_name = 'li7'
      new_frac = 3.135858e-9
      pgstar_flag = .true.

/ ! end of star_job namelist

&controls

      use_eosELM = .true.
      use_eosDT2 = .true.

      use_other_neu = .true.

      initial_mass = 1.0
      initial_z = 0.0148d0

      use_Type2_opacities = .true.
      Zbase = 0.0148d0

      log_L_lower_limit = -1
      use_Ledoux_criterion=.true.
      alpha_semiconvection = 4d-2
      thermohaline_coeff = 100d0
      mixing_length_alpha = 1.6

      okay_to_reduce_gradT_excess = .true.

      gradT_excess_f1 = 1d-4
      gradT_excess_f2 = 1d-2
      gradT_excess_age_fraction = 0.9d0
```

```
      gradT_excess_lambda1 = 1.0
      gradT_excess_beta1 = 0.5
      gradT_excess_lambda2 = 1.0
      gradT_excess_beta2 = 0.5
      gradT_excess_dlambda = 1
      gradT_excess_dbeta = 1

      cool_wind_full_on_T = 9.99d9
      hot_wind_full_on_T = 1d10
      cool_wind_RGB_scheme = 'Reimers'
      cool_wind_AGB_scheme = 'Blocker'
      RGB_to_AGB_wind_switch = 1d-4
      Reimers_scaling_factor = 0.3d0
      Blocker_scaling_factor = 0.7d0

/ ! end of controls namelist
```

Acknowledgment

First of all, I would like to thank Tositaka Kajino for supervising me during the Ph.D. course for five years. He introduced me to the exciting world of nuclear and particle astrophysics. I thank Motohiko Kusakabe for hosting my stay in Beijing and educating me about cosmology and stellar physics. His contribution to the collaborative research projects was indispensable, and I enjoyed my stay at Beijing as a research assistant and scientific discussion there. I am thankful to A. Baha Balantekin for hosting my stay in Madison and having discussions from the viewpoint of particle physics, Michael A. Famiano for teaching me nuclear physics in plasma, and Ken'ichi Nomoto for teaching me stellar physics. I am also grateful to Grant J. Mathews for hosting my stay in South Bend, and Toshio Suzuki and Michio Honma for providing their data on electron capture rates.

I was encouraged by colleagues at Division of Science, National Astronomical Observatory of Japan and School of Physics, Beihang University. Especially, I enjoyed conversation with Hirokazu Sasaki, Yudong Luo, Yuta Yamazaki, Xingqun Yao, and Zhenyu He. I am looking forward to collaborating with them even after getting the degree.

Finally, I thank Motoki and Akari for allowing me to be a 27-year-old student and supporting my daily life. I wish I could show this thesis to Iyoko.

This study is supported by JSPS KAKENHI Grant Number JP19J12892.

References

Aaboud, M., Aad, G., Abbott, B., et al. 2018, Journal of High Energy Physics, 2018, 126
Aad, G., Abbott, B., Abdallah, J., et al. 2011, Physics Letters B, 705, 294
Aad, G., Abajyan, T., Abbott, B., et al. 2013, Physical Review Letters, 110, 011802
Aaltonen, T., Adelman, J., Akimoto, T., et al. 2008, Physical Review Letters, 101, 181602
Abbott, B. P., Abbott, R., Abbott, T. D., et al. 2016, Physical Review Letters, 116, 061102
Aboubrahim, A., Ibrahim, T., Itani, A., et al. 2014, Physical Review D, 89, 055009
Adams, J. B., Ruderman, M. A., & Woo, C.-H. 1963, Physical Review, 129, 1383
Adamów, M., Niedzielski, A., Villaver, E., et al. 2014, Astronomy & Astrophysics, 569, A55
Aguilera-Gómez, C., Chanamé, J., Pinsonneault, M. H., et al. 2016, The Astrophysical Journal, 833, L24
Ahmad, Q. R., Allen, R. C., Andersen, T. C., et al. 2001, Physical Review Letters, 87, 071301
Aker, M., Altenmüller, K., Arenz, M., et al. 2019, Physical Review Letters, 123, 221802
Alastuey, A., & Jancovici, B. 1978, The Astrophysical Journal, 226, 1034
Arkani-Hamed, N., Dimopoulos, S., & Dvali, G. 1998, Physics Letters B, 429, 263
Anastassopoulos, V., Aune, S., Barth, K., et al. 2017, Nature Physics, 13, 584
Anders, E., & Grevesse, N. 1989, Geochimica et Cosmochimica Acta, 53, 197
Anderson, R. I., Saio, H., Ekström, S., et al. 2016, Astronomy & Astrophysics, 591, A8
Angulo, C., Arnould, M., Rayet, M., et al. 1999, Nuclear Physics A, 656, 3
Aprile, E., Aalbers, J., Agostini, F., et al. 2020, Physical Review D, 102, 072004
Arceo-Díaz, S., Schröder, K.-P., Zuber, K., et al. 2015, Astroparticle Physics, 70, 1
Arnould, M., & Goriely, S. 2020, Progress in Particle and Nuclear Physics, 112, 103766
Arpesella, C., Back, H. O., Balata, M., et al. 2008, Physical Review Letters, 101, 091302
Asplund, M., Grevesse, N., & Sauval, A. J. 2005, Cosmic Abundances as Records of Stellar Evolution and Nucleosynthesis, 25
Asplund, M., Grevesse, N., Sauval, A. J., et al. 2009, Annual Review of Astronomy and Astrophysics, 47, 481

Atkinson, R. d'Escourt. 1931, The Astrophysical Journal, 73, 250
Ayala, A., D'olivo, J. C., & Torres, M. 1999, Physical Review D, 59, 111901
Ayala, A., Domínguez, I., Giannotti, M., et al. 2014, Physical Review Letters, 113, 191302
Bahcall, J. N. 1962, Physical Review, 128, 1297
Balantekin, A. B., & Kayser, B. 2018, Annual Review of Nuclear and Particle Science, 68, 313
Barger, V., Han, T., Kao, C., et al. 1999, Physics Letters B, 461, 34
Baumgardt, H., Hilker, M., Sollima, A., et al. 2019, Monthly Notices of the Royal Astronomical Society, 482, 5138
Beda, A. G., Brudanin, V. B., Egorov, V. G., et al. 2013, Physics of Particles and Nuclei Letters, 10, 139
Bedding, T. R., Mosser, B., Huber, D., et al. 2011, Nature, 471, 608
Bellazzini, M., Ferraro, F. R., & Pancino, E. 2001, The Astrophysical Journal, 556, 635
Berdnikov, L. N., Dambis, A. K., & Vozyakova, O. V. 2000, Astronomy & Astrophysics Supplement Series, 143, 211
Bernstein, J., Ruderman, M., & Feinberg, G. 1963, Physical Review, 132, 1227
Bertulani, C. A., & Kajino, T. 2016, Progress in Particle and Nuclear Physics, 89, 56
Bethe, H. A. 1939, Physical Review, 55, 434
Bionta, R. M., Blewitt, G., Bratton, C. B., et al. 1987, Physical Review Letters, 58, 1494
Blinnikov, S. I. & Dunina-Barkovskaya, N. V. 1994, Monthly Notices of the Royal Astronomical Society, 266, 289
Bono, G., Castellani, V., & Marconi, M. 2000, The Astrophysical Journal, 529, 293
Bono, G., Caputo, F., Cassisi, S., et al. 2000, The Astrophysical Journal, 543, 955
Braaten, E. & Segel, D. 1993, Physical Review D, 48, 1478
Brown, J. A., Sneden, C., Lambert, D. L., et al. 1989, The Astrophysical Journal Supplement Series, 71, 293
Brunish, W. M., & Becker, S. A. 1990, The Astrophysical Journal, 351, 258
Buder, S., Asplund, M., Duong, L., et al. 2018, Monthly Notices of the Royal Astronomical Society, 478, 4513
Burbidge, E. M., Burbidge, G. R., Fowler, W. A., et al. 1957, Reviews of Modern Physics, 29, 547
Busso, M., Wasserburg, G. J., Nollett, K. M., et al. 2007, The Astrophysical Journal, 671, 802
Cameron, A. G. W. & Fowler, W. A. 1971, The Astrophysical Journal, 164, 111
Capozzi, F. & Raffelt, G. 2020, Physical Review D, 102, 083007

Casey, A. R., Ruchti, G., Masseron, T., et al. 2016, Monthly Notices of the Royal Astronomical Society, 461, 3336

Cassisi, S., Castellani, V., Degl'Innocenti, S., et al. 2000, Physics Letters B, 481, 323

Castilho, B. V., Gregorio-Hetem, J., Spite, F., et al. 2000, Astronomy & Astrophysics, 364, 674

Caughlan, G. R. & Fowler, W. A. 1988, Atomic Data and Nuclear Data Tables, 40, 283

Charbonnel, C. & Zahn, J.-P. 2007, Astronomy & Astrophysics, 467, L15

Charbonnel, C. & Lagarde, N. 2010, Astronomy & Astrophysics, 522, A10

Charbonnel, C., Lagarde, N., Jasniewicz, G., et al. 2020, Astronomy & Astrophysics, 633, A34

Chiaverini, J., Smullin, S. J., Geraci, A. A., et al. 2003, Physical Review Letters, 90, 151101

Choplin, A., Coc, A., Meynet, G., et al. 2017, Astronomy & Astrophysics, 605, A106

Cox, J. P. 1980, Theory of Stellar Pulsation (Princeton: Princeton University Press)

Cowan, C. L., Reines, F., & Harrison, F. B. 1954, Physical Review, 96, 1294

Cowan, C. L., Reines, F., Harrison, F. B., et al. 1956, Science, 124, 103

Cox, J. P. & Giuli, R. T. 1968, Principles of stellar structure, by J.P. Cox and R. T. Giuli. New York: Gordon and Breach, 1968

Danby, G., Gaillard, J.-M., Goulianos, K., et al. 1962, Physical Review Letters, 9, 36

Daraktchieva, Z., Amsler, C., Avenier, M., et al. 2005, Physics Letters B, 615, 153

Dearborn, D. S. P., Schramm, D. N., & Steigman, G. 1986, Physical Review Letters, 56, 26

deBoer, R. J., Görres, J., Wiescher, M., et al. 2017, Reviews of Modern Physics, 89, 035007

Deepak & Reddy, B. E. 2019, Monthly Notices of the Royal Astronomical Society, 484, 2000

de Jager, C., Nieuwenhuijzen, H., & van der Hucht, K. A. 1988, Astronomy & Astrophysics Supplement Series, 72, 259

Derbin, A. I., Chernyĭ, A. V., Popeko, L. A., et al. 1993, Soviet Journal of Experimental and Theoretical Physics Letters, 57, 768

Dicus, D. A. 1972, Physical Review D, 6, 941

Dohm-Palmer, R. C., & Skillman, E. D. 2002, The Astronomical Journal, 123, 1433

DONUT Collaboration, Kodama, K., Ushida, N., et al. 2001, Physics Letters B, 504, 218

Dyson, F. W., Eddington, A. S., & Davidson, C. 1920, Philosophical Transactions of the Royal Society of London Series A, 220, 291

Eddington, A. S. 1920, Nature, 106, 14

Eichler, D., Livio, M., Piran, T., et al. 1989, Nature, 340, 126

Einstein, A. 1905, Annalen der Physik, 322, 891

Einstein, A. 1915, Sitzungsberichte der Königlich Preußischen Akademie der Wissenschaften, 831

Einstein, A. 1916, Annalen der Physik, 354, 769

Einstein, A. 1916, Sitzungsberichte der Königlich Preußischen Akademie der Wissenschaften, 688

Ekström, S., Georgy, C., Eggenberger, P., et al. 2012, Astronomy & Astrophysics, 537, A146

Englert, F., & Brout, R. 1964, Physical Review Letters, 13, 321

Evans, N. R. 1993, The Astronomical Journal, 105, 1956

Ferguson, J. W., Alexander, D. R., Allard, F., Barman, T., Bodnarik, J. G., Hauschildt, P. H., Heffner-Wong, A., & Tamanai, A. 2005, The Astrophysical Journal, 623, 585

Fermi-LAT Collaboration, Ajello, M., Baldini, L., et al. 2012, Journal of Cosmology and Astroparticle Physics, 2012, 012

Fukuda, Y., Hayakawa, T., Ichihara, E., et al. 1998, Physical Review Letters, 81, 1562

Fuller, G. M., Fowler, W. A., & Newman, M. J. 1985, The Astrophysical Journal, 293, 1

Friedland, A., Giannotti, M., & Wise, M. 2013, Physical Review Letters, 110, 061101

Gamow, G. 1928, Zeitschrift fur Physik, 51, 204

Gamow, G. 1938, Physical Review, 53, 595

Gando, A., Gando, Y., Hachiya, T., et al. 2016, Physical Review Letters, 117, 082503

Geraci, A. A., Smullin, S. J., Weld, D. M., et al. 2008, Physical Review D, 78, 022002

Giunti, C., & Studenikin, A. 2015, Reviews of Modern Physics, 87, 531

Gonzalez, O. A., Zoccali, M., Monaco, L., et al. 2009, Astronomy & Astrophysics, 508, 289

Haft, M., Raffelt, G., & Weiss, A. 1994, The Astrophysical Journal, 425, 222

Halabi, G. M., El Eid, M. F., & Champagne, A. 2012, The Astrophysical Journal, 761, 10

Hall, L. J. & Smith, D. 1999, Physical Review D, 60, 085008

Hanhart, C., Pons, J. A., Phillips, D. R., et al. 2001, Physics Letters B, 509, 1

Hannestad, S., & Raffelt, G. G. 2003, Physical Review D, 67, 125008

Hansen, B. M. S., Richer, H., Kalirai, J., et al. 2015, The Astrophysical Journal, 809, 141

Heger, A., Friedland, A., Giannotti, M., et al. 2009, The Astrophysical Journal, 696, 608

Higgs, P. W. 1964, Physical Review Letters, 13, 508

Hirata, K., Kajita, T., Koshiba, M., et al. 1987, Physical Review Letters, 58, 1490

Hoyle, C. D., Schmidt, U., Heckel, B. R., et al. 2001, Physical Review Letters, 86, 1418

Hoyle, C. D., Kapner, D. J., Heckel, B. R., et al. 2004, Physical Review D, 70, 042004

Huang, W., Gies, D. R., & McSwain, M. V. 2010, The Astrophysical Journal, 722, 605

Hulse, R. A., & Taylor, J. H. 1975, The Astrophysical Journal, 195, L51
Iben, I. 1967, The Astrophysical Journal, 147, 624
Iglesias, C. A., & Rogers, F. J. 1993, The Astrophysical Journal, 412, 752
Iglesias, C. A., & Rogers, F. J. 1996, The Astrophysical Journal, 464, 943
Inman, C. L., & Ruderman, M. A. 1964, The Astrophysical Journal, 140, 1025
Itoh, N., Totsuji, H., Ichimaru, S., & Dewitt, H. E. 1979, The Astrophysical Journal, 234, 1079
Itoh, N., Hayashi, H., Nishikawa, A., et al. 1996, The Astrophysical Journal Supplement Series, 102, 411
Iwamoto, N., Qin, L., Fukugita, M., et al. 1995, Physical Review D, 51, 348
Kaluza, T. 1921, Sitzungsberichte der Königlich Preußischen Akademie der Wissenschaften (Berlin), 966
Kapner, D. J., Cook, T. S., Adelberger, E. G., et al. 2007, Physical Review Letters, 98, 021101
Kepler, J. 1609, Astronomia nova
Kepler, J. 1619, Harmonices mvndi
Kippenhahn, R., Weigert, A., & Weiss, A. 2012, Stellar Structure and Evolution (Berlin, Heidelberg: Springer)
Klein, O. 1926, Zeitschrift fur Physik, 37, 895
Krauss, L. M., Moody, J. E., & Wilczek, F. 1984, Physics Letters B, 144, 391
Kumar, Y. B., Reddy, B. E., & Lambert, D. L. 2011, The Astrophysical Journal, 730, L12
Kumar, Y. B., Reddy, B. E., Campbell, S. W., et al. 2020, Nature Astronomy, doi:10.1038/s41550-020-1139-7
Kunz, R., Fey, M., Jaeger, M., et al. 2002, The Astrophysical Journal, 567, 643
Kusakabe, M., Balantekin, A. B., Kajino, T., et al. 2013, Physical Review D, 87, 085045
Lagarde, N., Decressin, T., Charbonnel, C., et al. 2012, Astronomy & Astrophysics, 543, A108
Langanke, K, & Martínez-Pinedo, 2000, Nuclear Physics A, 673, 481
Lattanzio, J. C., Siess, L., Church, R. P., et al. 2015, Monthly Notices of the Royal Astronomical Society, 446, 2673
Lebzelter, T., Uttenthaler, S., Busso, M., et al. 2012, Astronomy & Astrophysics, 538, A36
Ledoux, P. 1947, The Astrophysical Journal, 105, 305
Lee, J. G., Adelberger, E. G., Cook, T. S., et al. 2020, Physical Review Letters, 124, 101101
Le Verrier, U. J. 1859, Annales de l'Observatoire de Paris, 5, 1
Liu, D. W., Ashie, Y., Fukuda, S., et al. 2004, Physical Review Letters, 93, 021802

Lodders, K. 2020, Solar Elemental Abundances, in The Oxford Research Encyclopedia of Planetary Science, Oxford University Press

Long, J. C., Chan, H. W., & Price, J. C. 1999, Nuclear Physics B, 539, 23

Maki, Z., Nakagawa, M., & Sakata, S. 1962, Progress of Theoretical Physics, 28, 870

Mandelstam, S. 1958, Physical Review, 112, 1344

Martell, S. L. & Shetrone, M. D. 2013, Monthly Notices of the Royal Astronomical Society, 430, 611

McQuinn, K. B. W., Skillman, E. D., Dalcanton, J. J., et al. 2011, The Astrophysical Journal, 740, 48

Miller Bertolami, M. M. 2014, Astronomy & Astrophysics, 562, A123

Mohapatra, R. N., & Senjanovic, G. 1980, Physical Review Letters, 44, 912

Monaco, L., Villanova, S., Moni Bidin, C., et al. 2011, Astronomy & Astrophysics, 529, A90

Monaco, L., Boffin, H. M. J., Bonifacio, P., et al. 2014, Astronomy & Astrophysics, 564, L6

Morel, P., Provost, J., Pichon, B., et al. 2010, Astronomy & Astrophysics, 520, A41

Mori, K., Balantekin, A. B., Kajino, T., et al. 2020, The Astrophysical Journal, 901, 115

Mori, K., Kusakabe, M., Balantekin, A. B., et al. 2020, arXiv:2009.00293

Murata, J. & Tanaka, S. 2015, Classical and Quantum Gravity, 32, 033001

Newton, I. 1687, Philosophiae Naturalis Principia Mathematica

Neilson, H. R., Cantiello, M., & Langer, N. 2011, Astronomy & Astrophysics, 529, L9

Neilson, H. R., & Lester, J. B. 2008, The Astrophysical Journal, 684, 569

Oda, T., Hino, M., Muto, K., Takahara, M., & Sato, K. 1994, Atomic Data and Nuclear Data Tables, 56, 231

Overduin, J. M. & Wesson, P. S. 1997, Physics Reports, 283, 303

Palacios, A., Talon, S., Charbonnel, C., et al. 2003, Astronomy & Astrophysics, 399, 603

Paxton, B., Bildsten, L., Dotter, A., et al. 2011, The Astrophysical Journal Supplement Series, 192, 3

Paxton, B., Cantiello, M., Arras, P., et al. 2013, The Astrophysical Journal Supplement Series, 208, 4

Paxton, B., Marchant, P., Schwab, J., et al. 2015, The Astrophysical Journal Supplement Series, 220, 15

Paxton, B., Schwab, J., Bauer, E. B., et al. 2018, The Astrophysical Journal Supplement Series, 234, 34

Paxton, B., Smolec, R., Schwab, J., et al. 2019, arXiv e-prints, arXiv:1903.01426

Petrosian, V., Beaudet, G., & Salpeter, E. E. 1967, Physical Review, 154, 1445
Raffelt, G. G., & Dearborn, D. S. P. 1987, Physical Review D, 36, 2211
Raffelt, G. G., & Dearborn, D. S. P. 1988, Physical Review D, 37, 549
Raffelt, G. G. 1990, The Astrophysical Journal, 365, 559
Raffelt, G., & Weiss, A. 1992, Astronomy & Astrophysics, 264, 536
Raffelt, G. & Weiss, A. 1995, Physical Review D, 51, 1495
Raffelt, G. G. 1996, Stars as laboratories for fundamental physics: the astrophysics of neutrinos
Reimers, D. 1975, Memoires of the Societe Royale des Sciences de Liege, 8, 369
Ressell, M. T. & Turner, M. S. 1990, Comments on Astrophysics, 14, 323
Rogers, F. J., & Nayfonov, A. 2002, The Astrophysical Journal, 576, 1064
Ruchti, G. R., Fulbright, J. P., Wyse, R. F. G., et al. 2011, The Astrophysical Journal, 743, 107
Sackmann, I.-J. & Boothroyd, A. I. 1999, The Astrophysical Journal, 510, 217
Sandage, A. R., & Schwarzschild, M. 1952, The Astrophysical Journal, 116, 463
Sandage, A., & Tammann, G. A. 2006, Annual Review of Astronomy and Astrophysics, 44, 93
Sato, K. 1975, Progress of Theoretical Physics, 54, 1325
Sato, K., & Sato, H. 1975, Progress of Theoretical Physics, 54, 1564
Schaller, G., Schaerer, D., Meynet, G., et al. 1992, Astronomy & Astrophysics Supplement Series, 96, 269
Schechter, J., & Valle, J. W. F. 1980, Physical Review D, 22, 2227
Schwab, J. 2020, The Astrophysical Journal, 901, L18
Serenelli, A., Weiss, A., Cassisi, S., et al. 2017, Astronomy & Astrophysics, 606, A33
Shrock, R. E. 1982, Nuclear Physics B, 206, 359
Siess, L. & Livio, M. 1999, Monthly Notices of the Royal Astronomical Society, 308, 1133
Silva Aguirre, V., Ruchti, G. R., Hekker, S., et al. 2014, The Astrophysical Journal, 784, L16
Simonucci, S., Taioli, S., Palmerini, S., et al. 2013, The Astrophysical Journal, 764, 118
Singh, R., Reddy, B. E., & Kumar, Y. B. 2019, Monthly Notices of the Royal Astronomical Society, 482, 3822
Singh, R., Reddy, B. E., Bharat Kumar, Y., et al. 2019, The Astrophysical Journal, 878, L21
Sirunyan, A. M., Tumasyan, A., Adam, W., et al. 2018, Physical Review D, 97, 092005
Smiljanic, R., Franciosini, E., Bragaglia, A., et al. 2018, Astronomy & Astrophysics, 617, A4

Smullin, S. J., Geraci, A. A., Weld, D. M., et al. 2005, Physical Review D, 72, 122001
Straniero, O., Dominguez, I., Piersanti, L., et al. 2019, The Astrophysical Journal, 881, 158
Suda, T., Hirschi, R., & Fujimoto, M. Y. 2011, The Astrophysical Journal, 741, 61
Sushkov, A. O., Kim, W. J., Dalvit, D. A. R., et al. 2011, Physical Review Letters, 107, 171101
Tan, W.-H., Yang, S.-Q., Shao, C.-G., et al. 2016, Physical Review Letters, 116, 131101
Tan, W.-H., Du, A.-B., Dong, W.-C., et al. 2020, Physical Review Letters, 124, 051301
Tanabashi, M., Hagiwara, K., Hikasa, K., et al. 2018, Physical Review D, 98, 030001
Tatischeff, V. & Thibaud, J.-P. 2007, Astronomy & Astrophysics, 469, 265
Terasawa, N., Kawasaki, M., & Sato, K. 1988, Nuclear Physics B, 302, 697
Timmes, F. X., & Swesty, F. D. 2000, The Astrophysical Journal Supplement Series, 126, 501
Ting, Y.-S., Hawkins, K., & Rix, H.-W. 2018, The Astrophysical Journal, 858, L7
Tu, L.-C., Guan, S.-G., Luo, J., et al. 2007, Physical Review Letters, 98, 201101
Turner, D. G. 1996, Journal of the Royal Astronomical Society of Canada, 90, 82
Turner, D. G., & Burke, J. F. 2002, The Astronomical Journal, 124, 2931
Unno, W., Osaki, Y., Ando, H., et al. 1989, Nonradial oscillations of stars, Tokyo: University of Tokyo Press, 1989, 2nd ed.
Valle, G., Marconi, M., Degl'Innocenti, S., et al. 2009, Astronomy & Astrophysics, 507, 1541
Ventura, P., & D'Antona, F. 2010, Monthly Notices of the Royal Astronomical Society, 402, L72
Vescovi, D., Piersanti, L., Cristallo, S., et al. 2019, Astronomy & Astrophysics, 623, A126
Viaux, N., Catelan, M., Stetson, P. B., et al. 2013, Astronomy & Astrophysics, 558, A12
Viaux, N., Catelan, M., Stetson, P. B., et al. 2013, Physical Review Letters, 111, 231301
Vidyakin, G. S., Vyrodov, V. N., Gurevich, I. I., et al. 1992, Soviet Journal of Experimental and Theoretical Physics Letters, 55, 206
Vrard, M., Mosser, B., & Samadi, R. 2016, Astronomy & Astrophysics, 588, A87
Wallerstein, G. & Sneden, C. 1982, The Astrophysical Journal, 255, 577
Wong, H. T., Li, H. B., Lin, S. T., et al. 2007, Physical Review D, 75, 012001
Xu, H. Y., & Li, Y. 2004, Astronomy & Astrophysics, 418, 213
Xu, H. Y., & Li, Y. 2004, Astronomy & Astrophysics, 418, 225
Yan, H.-L., Shi, J.-R., Zhou, Y.-T., et al. 2018, Nature Astronomy, 2, 790
Yan, H.-L., Zhou, Y.-T., Zhang, X., et al. 2020, Nature Astronomy
Yanagida, T. 1980, Progress of Theoretical Physics, 64, 1103

Yang, S.-Q., Zhan, B.-F., Wang, Q.-L., et al. 2012, Physical Review Letters, 108, 081101
Zaidi, M. H. 1965, Nuovo Cimento A Serie, 40, 502
Zyla, P. A., et al. 2020, Progress of Theoretical and Experimental Physics, 2020, 083C01